

# Accurate frozen-density embedding potentials as a first step towards a subsystem description of covalent bonds

Samuel Fux,<sup>1</sup> Christoph R. Jacob,<sup>1,a),b)</sup> Johannes Neugebauer,<sup>2,a)</sup> Lucas Visscher,<sup>3</sup> and Markus Reiher<sup>1</sup>

<sup>1</sup>Laboratorium für Physikalische Chemie, ETH Zurich, Wolfgang-Pauli-Strasse 10, 8093 Zurich, Switzerland

<sup>2</sup>Gorlaeus Laboratories, Leiden Institute of Chemistry, Universiteit Leiden, 2300 RA Leiden, The Netherlands

<sup>3</sup>Amsterdam Center for Multiscale Modeling, VU University Amsterdam, De Boelelaan 1083, 1081 HV Amsterdam, The Netherlands

(Received 21 January 2010; accepted 10 March 2010; published online 22 April 2010)

The frozen-density embedding (FDE) scheme [Wesolowski and Warshel, *J. Phys. Chem.* **97**, 8050 (1993)] relies on the use of approximations for the kinetic-energy component  $v_T[\rho_1, \rho_2]$  of the embedding potential. While with approximations derived from generalized-gradient approximation kinetic-energy density functional weak interactions between subsystems such as hydrogen bonds can be described rather accurately, these approximations break down for bonds with a covalent character. Thus, to be able to directly apply the FDE scheme to subsystems connected by covalent bonds, improved approximations to  $v_T$  are needed. As a first step toward this goal, we have implemented a method for the numerical calculation of accurate references for  $v_T$ . We present accurate embedding potentials for a selected set of model systems, in which the subsystems are connected by hydrogen bonds of various strength (water dimer and F–H–F<sup>-</sup>), a coordination bond (ammonia borane), and a prototypical covalent bond (ethane). These accurate potentials are analyzed and compared to those obtained from popular kinetic-energy density functionals. © 2010 American Institute of Physics. [doi:10.1063/1.3376251]

## I. INTRODUCTION

The quantum chemical description of biomolecules is challenging because of the large size of such molecules. Such calculations also produce a large amount of data, which become increasingly difficult to interpret. Subsystem approaches, in which a large system is divided into its constituting fragments, offer a theoretical description which is not only more efficient but also provides a picture that is much more accessible for a chemical interpretation (for recent reviews, see Refs. 1 and 2). Most prominent examples of such approaches are combined quantum mechanics/molecular mechanics schemes,<sup>3–7</sup> which allow one to focus on a specific region of interest, as well as methods for describing proteins in terms of their amino acid building blocks,<sup>8–10</sup> in which all subsystems are treated on an equal footing.

The frozen-density embedding (FDE) scheme, which has been introduced by Wesolowski and Warshel<sup>11</sup> based on earlier work by Cortona,<sup>12</sup> is a very appealing realization of a subsystem approach within the framework of density-functional theory (DFT). It is based on a partitioning of the electron density  $\rho_{\text{tot}}(\mathbf{r})$  of the full system into the density  $\rho_1(\mathbf{r})$  of an active subsystem and the density  $\rho_2(\mathbf{r})$  of a frozen environment. A generalization to an arbitrary number of subsystems is straightforward (see, e.g., Refs. 13 and 14). For a

given frozen density  $\rho_2(\mathbf{r})$ , the electron density  $\rho_1(\mathbf{r})$  of the active subsystem can then be determined from a set of one-electron equations, in which the effect of the frozen environment is taken into account through an effective embedding potential given by

$$v_{\text{eff}}^{\text{embr}}[\rho_1, \rho_2](\mathbf{r}) = v_2^{\text{nuc}}(\mathbf{r}) + \int \frac{\rho_2(\mathbf{r}')}{|\mathbf{r} - \mathbf{r}'|} d^3r' + \frac{\delta E_{\text{xc}}[\rho_{\text{tot}}]}{\delta \rho_{\text{tot}}(\mathbf{r})} - \frac{\delta E_{\text{xc}}[\rho_1]}{\delta \rho_1(\mathbf{r})} + \underbrace{\frac{\delta T_s^{\text{nadd}}[\rho_1, \rho_2]}{\delta \rho_1(\mathbf{r})}}_{v_T[\rho_1, \rho_2]} \quad (1)$$

In this embedding potential,  $v_2^{\text{nuc}}(\mathbf{r})$  denotes the nuclear potential of the environment,  $E_{\text{xc}}[\rho]$  is the exchange-correlation (xc) energy functional and

$$T_s^{\text{nadd}}[\rho_1, \rho_2] = T_s[\rho_{\text{tot}}] - T_s[\rho_1] - T_s[\rho_2] \quad (2)$$

is the nonadditive kinetic energy functional.

The FDE scheme provides a subsystem description that is in principle exact. With the exact nonadditive kinetic-energy functional  $T_s^{\text{nadd}}[\rho_1, \rho_2]$ , the use of the above effective embedding potential would yield the exact density  $\rho_1(\mathbf{r})$  for the active subsystem, i.e., the resulting density  $\rho_1(\mathbf{r})$  is such that  $\rho_{\text{tot}}(\mathbf{r}) = \rho_1(\mathbf{r}) + \rho_2(\mathbf{r})$  is equal to the total electron density obtained from a Kohn-Sham (KS)-DFT calculation on the full system using the same (approximate) xc-functional. However, for this to be possible the frozen density  $\rho_2(\mathbf{r})$  has

<sup>a)</sup> Authors to whom correspondence should be addressed. Electronic mail: christoph.jacob@kit.edu and j.neugebauer@chem.leidenuniv.nl.

<sup>b)</sup> Present address: Karlsruhe Institute of Technology (KIT), Center for Functional Nanostructures, Wolfgang-Gaede-Str. 1a, 76131 Karlsruhe, Germany.

to be chosen such that it fulfills certain criteria,<sup>15,16</sup> which is in practice difficult to achieve. This problem will be discussed in more detail in Sec. II C.

Therefore, the FDE scheme can be employed in two different ways. First, it can be used as an effective environment model by using an approximate frozen density to model the environment.<sup>11,15</sup> In this case, it is possible to obtain an accurate description of an active subsystem of interest, but it will, in general, neither be possible to correct for deficiencies of the frozen density nor to describe a polarization of the environment density. This strategy has, for instance, successfully been applied to model solvent effects on molecular properties<sup>15,17–20</sup> and to account for environment effects on free energies in solution and in proteins.<sup>21–24</sup> Second, the FDE scheme can be used as a subsystem alternative to conventional KS-DFT calculations by iteratively exchanging the roles of the frozen and nonfrozen subsystems in the so-called freeze-and-thaw cycles.<sup>25</sup> This allows the frozen density to change, so that in principle it should be possible to obtain subsystem densities that add up to the correct total electron densities, even if the initial densities do not fulfill the required criteria. However, whether such a freeze-and-thaw procedure eventually converges to the correct total density has recently been questioned.<sup>26</sup> Such a subsystem DFT formulation can be generalized to time-dependent (TD) DFT to allow for a description of coupled electronic excitations<sup>27,28</sup> as well as the calculation of polarizabilities and other general response properties,<sup>29</sup> following the earlier work on TDDFT within the two-partition FDE context.<sup>30,31</sup> Of course, intermediate setups, in which only parts of the frozen density are updated, are also possible.<sup>14</sup>

Even though FDE is in principle exact, the exact nonadditive kinetic-energy functional  $T_s^{\text{nonadd}}[\rho_1, \rho_2]$  is not available in practical calculations. The evaluation of the nonadditive kinetic energy for the total density  $T_s[\rho_{\text{tot}}]$  requires the knowledge of the KS orbitals of the total system, but only those of the subsystems are available in FDE calculations. Therefore, in practical calculations the nonadditive kinetic energy and its contribution to the embedding potential,

$$v_T[\rho_1, \rho_2] = \frac{\delta T_s^{\text{nonadd}}[\rho_1, \rho_2]}{\delta \rho_1} = \frac{\delta T_s[\rho_{\text{tot}}]}{\delta \rho_{\text{tot}}} - \frac{\delta T_s[\rho_1]}{\delta \rho_1}, \quad (3)$$

have to be approximated. Usually, this is done by applying an approximate kinetic-energy density functional for evaluating the functional derivative of  $T_s[\rho]$ . Both the local-density approximation (LDA), corresponding to the well-known Thomas–Fermi (TF) functional,<sup>32,33</sup> as well as generalized-gradient approximation (GGA) functionals (for an overview, see Ref. 34) have been used in this context.<sup>35,36</sup> In particular, when the popular PW91k kinetic-energy functional<sup>37</sup> is used to approximate  $v_T$  [this approximation has also been referred to as GGA97 (Ref. 35)], accurate results can be obtained for van der Waals complexes<sup>38–40</sup> as well as for hydrogen-bonded systems.<sup>31,35,36,41,42</sup> Recently, more advanced approximations to  $v_T$ , which are not derived from a parent kinetic-energy functional but which try to approximate the nonadditive kinetic-energy or its functional derivative directly (the so-called *nondecomposable* approximations)—either as an explicit density functional or

as an implicit functional—have also been proposed.<sup>43,44</sup>

However, the applicability of the currently available approximations to  $v_T$  is mostly limited to van der Waals complexes and subsystems connected by hydrogen bonds. If the interaction between the subsystems has a larger covalent character, the available approximations for  $v_T$  break down.<sup>45</sup> For instance, it was recently shown that there are severe deficiencies already for the coordination bond in ammonia borane<sup>46</sup> as well as for the weak covalent bond in complexes of noble gas atoms and AuF.<sup>47</sup> Furthermore, while the available approximations work reasonably well for complexes where bonding is mainly ionic, they completely break down for transition metal complexes with more challenging bonding situations, such as carbonyl complexes where  $\pi$ -backbonding plays an important role.<sup>46</sup> However, in particular for a subsystem description of biological systems, it is usually necessary to treat subsystems connected by covalent bonds. To allow for a rigorous subsystem description of proteins in terms of their amino acid building blocks, a three-partition FDE scheme, in which capping groups are introduced to model covalent bonds between subsystems, has recently been proposed.<sup>48</sup> However, such a scheme introduces additional approximations and can only be considered as a pragmatic solution for circumventing the insufficiencies of current approximations to  $v_T$ .

Thus, to extend to applicability of FDE beyond hydrogen-bonded systems, the development of improved approximations to  $v_T$  is mandatory.<sup>45</sup> A promising strategy to achieve this goal is to investigate exact properties of  $v_T$ , which can then be used as guidance in constructing approximations. In particular, the knowledge of accurate reference potentials of selected model systems is invaluable for understanding such exact properties of  $v_T$  as well as for identifying shortcomings of current approximations. Such a strategy has already been very successful in the development of approximations to the xc-potential, where the consideration of exact properties of the xc-potential led, for instance, to the widely used SAOP potential<sup>49–51</sup> or where the comparison to accurate xc-potentials inspired the development of the KTN family of xc-functionals.<sup>52,53</sup> For approximations to  $v_T$  much attention has recently been paid to the investigation of exact properties and the development of approximations enforcing these properties.<sup>43,44</sup> However, exact reference potentials for  $v_T$  are so far only known for special limits—such as infinitely separated subsystems<sup>43</sup> or close to the nuclei of the frozen subsystems<sup>44</sup>—and for four-electron systems.<sup>54</sup> As a first step toward the development of improved approximations to  $v_T$ , in this paper, we built on these efforts by numerically calculating accurate reference potentials for  $v_T$  and the effective embedding potential for arbitrary systems, which allows for a spatially resolved comparison to approximate potentials.

This work is organized as follows. In Sec. II, the theoretical background and the computational methodology used for the calculation of accurate embedding potentials are presented. This is followed by a careful assessment of the accuracy of this methodology. The quality of the electron density resulting from the reconstructed potentials is analyzed in Sec. III, whereas the shape and the accuracy of the potentials

themselves are discussed in Sec. IV. Finally, in Sec. V the calculated accurate embedding potentials are compared to approximate embedding potentials obtained from different kinetic-energy density functionals. Concluding remarks are given in Sec. VI.

## II. THEORY AND COMPUTATIONAL METHODOLOGY

### A. Calculation of accurate $v_T[\rho_1, \rho_2]$

The kinetic-energy component  $v_T[\rho_1, \rho_2]$  of the effective embedding potential depends on the functional derivative of the noninteracting kinetic energy  $T_s[\rho]$  evaluated for the total electron density  $\rho_{\text{tot}}(\mathbf{r})$  and for the electron density of subsystem 1,  $\rho_1(\mathbf{r})$  [see Eq. (3)]. These functional derivatives  $(\delta T_s[\rho]/\delta\rho)|_{\rho=\rho_n(\mathbf{r})}$  (where  $n=1$  or tot) are related to the corresponding Kohn–Sham potentials  $v_s[\rho_n](\mathbf{r})$ ,<sup>43</sup> where  $v_s[\rho_n](\mathbf{r})$  denotes the Kohn–Sham potential that has the electron density  $\rho_n(\mathbf{r})$  as its ground-state density. The unique existence of such a potential is guaranteed for all  $v_s$ -representable electron densities by the Hohenberg–Kohn theorem.<sup>55</sup> Note that the functional derivative  $\delta T_s[\rho]/\delta\rho$  is not defined for electron densities that are not  $v_s$ -representable.<sup>56–58</sup> For the potential  $v_s[\rho_n](\mathbf{r})$ , the electron density  $\rho_n(\mathbf{r})$  minimizes the total-energy functional of a system of noninteracting electrons,

$$E_{v_s}[\rho] = T_s[\rho] + \int v_s[\rho_n](\mathbf{r})\rho(\mathbf{r})d^3r. \quad (4)$$

The corresponding Euler–Lagrange equation for the minimization of this total-energy functional (under the constraint that  $\rho$  integrates to the correct number of electrons) reads

$$\left. \frac{\delta T_s[\rho]}{\delta\rho} \right|_{\rho=\rho_n(\mathbf{r})} + v_s[\rho_n](\mathbf{r}) = \mu_s^{\rho_n}, \quad (5)$$

which allows one to evaluate  $\delta T_s[\rho]/\delta\rho$  as

$$\left. \frac{\delta T_s[\rho]}{\delta\rho} \right|_{\rho=\rho_n(\mathbf{r})} = -v_s[\rho_n](\mathbf{r}) + \mu_s^{\rho_n}. \quad (6)$$

Using this result, we can rewrite  $v_T[\rho_1, \rho_2](\mathbf{r})$  as

$$\begin{aligned} v_T[\rho_1, \rho_2](\mathbf{r}) &= \left. \frac{\delta T_s^{\text{nadd}}[\rho_1, \rho_2]}{\delta\rho_1} \right|_{\rho_1=\rho_1(\mathbf{r})} \\ &= v_s[\rho_1] - v_s[\rho_{\text{tot}}] + \Delta\mu, \end{aligned} \quad (7)$$

where  $\Delta\mu = \mu^{\rho_{\text{tot}}} - \mu^{\rho_1}$  only leads to a constant shift of the potential. This exact expression was applied to Ref. 43 to investigate the exact form of  $v_T[\rho_1, \rho_2]$  in the limit of a large separation of the subsystems.

If we choose  $\rho_{\text{tot}}(\mathbf{r})$  as the electron density obtained from a KS-DFT calculation on the full system employing an approximate exchange–correlation potential, the potential  $v_s[\rho_{\text{tot}}]$ , which is related to the second term in Eq. (3), is given by

$$v_s[\rho_{\text{tot}}] = v_{\text{ext}}(\mathbf{r}) + \int \frac{\rho_{\text{tot}}(\mathbf{r}')}{|\mathbf{r} - \mathbf{r}'|} d^3r' + \frac{\delta E_{\text{xc}}[\rho_{\text{tot}}]}{\delta\rho_{\text{tot}}(\mathbf{r})}, \quad (8)$$

i.e., it is directly available as the sum of the nuclear potential, the electronic Coulomb potential, and the (approximate)

exchange–correlation potential of the full system. In contrast, the first term  $v_s[\rho_1]$  in Eq. (7) is not easily accessible. For a given frozen electron density  $\rho_2(\mathbf{r})$ , and with  $\rho_{\text{tot}}(\mathbf{r})$  available from a calculation on the full system, the exact  $\rho_1(\mathbf{r})$  is given as  $\rho_1(\mathbf{r}) = \rho_{\text{tot}}(\mathbf{r}) - \rho_2(\mathbf{r})$ . However, the Kohn–Sham potential  $v_s[\rho_1]$ , that has this electron density as its ground-state electron density, is not known and has to be reconstructed. There is a wide variety of methods available to reconstruct the Kohn–Sham potential from a given electron density accurately.<sup>59–63</sup> Here and in the following, we use the term “accurate potential” instead of “exact potential” to point out that such reconstruction procedures are always prone to numerical errors. With such an accurate reconstructed potential  $\tilde{v}_s[\rho_1]$ , it is then possible to obtain an accurate  $\tilde{v}_T[\rho_1, \rho_2](\mathbf{r})$  as

$$\begin{aligned} \tilde{v}_T[\rho_1, \rho_2] &= \tilde{v}_s[\rho_1] - v_{\text{ext}}(\mathbf{r}) - \int \frac{\rho_{\text{tot}}(\mathbf{r}')}{|\mathbf{r} - \mathbf{r}'|} d^3r' - \frac{\delta E_{\text{xc}}[\rho_{\text{tot}}]}{\delta\rho_{\text{tot}}(\mathbf{r})} \\ &+ \Delta\mu. \end{aligned} \quad (9)$$

The accuracy of this  $\tilde{v}_T[\rho_1, \rho_2](\mathbf{r})$  solely relies on the accuracy of the reconstructed potential  $\tilde{v}_s[\rho_1]$ . If it was exact, a single embedding calculation using this  $\tilde{v}_T$  in the embedding potential of Eq. (1) would give the same result as a KS-DFT calculation of the full system.

### B. Potential reconstruction

For the reconstruction of the potential, we chose to use the direct optimization method of Wu and Yang<sup>62</sup> with an additional constraint which ensures that the obtained potentials are smooth, as proposed by Bulat *et al.*<sup>63</sup> The method of Wu and Yang starts with the definition of a Lagrangian functional  $W_s[v_s(\mathbf{r})]$ , depending on the sought potential,

$$W_s[v_s(\mathbf{r})] = 2 \sum_i^{N/2} \langle \phi_i | \hat{T} | \phi_i \rangle + \int v_s(\mathbf{r})[\rho(\mathbf{r}) - \rho_{\text{in}}(\mathbf{r})]d^3r, \quad (10)$$

where  $\rho_{\text{in}}(\mathbf{r})$  is the target electron density and  $\rho(\mathbf{r})$  and  $\{\phi_i(\mathbf{r})\}$  denote the electron density and the Kohn–Sham orbitals that result from  $v_s(\mathbf{r})$ , respectively. If the Lagrangian functional is maximized,  $W_s[v_s(\mathbf{r})]$  equals the kinetic energy  $T_s[\rho_{\text{in}}]$  and  $v_s(\mathbf{r})$  equals the sought Kohn–Sham potential  $v_s[\rho_{\text{in}}](\mathbf{r})$ . For a direct optimization, the potential  $v_s(\mathbf{r})$  is expanded into an initial guess  $v_0(\mathbf{r})$  and a linear combination of auxiliary functions  $g_t(\mathbf{r})$ , which model the difference between the initial guess and the final potential,

$$v_s(\mathbf{r}) = v_0(\mathbf{r}) + \sum_t b_t g_t(\mathbf{r}). \quad (11)$$

Due to this expansion of the potential, the problem now turned into an unconstrained maximization of  $W_s[v_s(\mathbf{r})]$  with respect to the expansion coefficients  $\{b_t\}$ . The first and the second derivatives of  $W_s[v_s(\mathbf{r})]$  with respect to the expansion coefficients  $\{b_t\}$  can be calculated analytically (expressions can be found in Ref. 62). This makes it possible to use a standard optimization algorithm, such as the Newton–Raphson method, for determining the expansion coefficients.

We have implemented the scheme of Wu and Yang for the reconstruction of a potential from a given input electron density in the Amsterdam density functional package ADF. In our implementation we decided to use the same set of normalized Slater-type fit functions that is used in ADF for the density fitting. As a convergence criterion for the potential reconstruction, we used the norm of the gradient of the Lagrangian functional  $W_s$  with respect to the coefficients  $b_t$ , i.e., the reconstruction is terminated when the gradient drops below a given threshold. In the determination of the Newton–Raphson steps, a truncated eigenvalue decomposition, in which eigenvalues smaller than  $10^{-6}$  are projected out, is used to invert the Hessian. To ensure the convergence of the Newton–Raphson minimization a shift between 0.0 and 1.0 (depending on the system) has been applied to the eigenvalues of the Hessian.

In general, the reconstruction of a potential from a given electron density does not always result in a final potential which is physically meaningful. The problem arises due to the finite basis set expansion used for representing the Kohn–Sham orbitals (and thus the electron density). If we use a finite basis set, infinitely many potentials may exist that reproduce the input electron density. This is not a contradiction to the first Hohenberg–Kohn theorem, which is only valid in the complete basis set limit. In general, the basis set expansion used for the potential will allow variations in the potential which lead to changes in the reconstructed potential that cannot be “seen” by the electron density. The result of the potential reconstruction is therefore somewhat arbitrary and can contain artifacts such as strong oscillations.<sup>64–68</sup> Several approaches for overcoming this problem have been proposed.<sup>63,65–67</sup> Here, we decided to follow the suggestion of Ref. 63 and introduce a regularization norm  $\|\nabla v_b(\mathbf{r})\|$  in the Lagrangian functional to ensure the smoothness of the reconstructed potentials,

$$\bar{W}_s[v(\mathbf{r})] = W_s[v_s(\mathbf{r})] + \lambda \|\nabla v_b(\mathbf{r})\|^2, \quad (12)$$

with

$$\|\nabla v_b(\mathbf{r})\|^2 = \sum_t \sum_u b_t b_u \langle g_t(\mathbf{r}) | \nabla^2 | g_u(\mathbf{r}) \rangle. \quad (13)$$

With this additional term in the Lagrangian, the squared norm of the gradient of the expansion-dependent term of the potential is minimized. If the reconstructed potential is not unique, the additional constraint ensures that the “smoothest” possible solution is chosen. However, if a too high value is used for  $\lambda$ , the smoothness constraint outweighs the requirement that the correct target electron density is obtained, and the reconstructed potential is no longer equivalent to the best possible solution. Therefore,  $\lambda$  has to be chosen large enough to ensure that among equivalent potentials, the smoothest one is chosen, but small enough to still obtain the correct target electron density. It is therefore important to determine the smallest possible value for  $\lambda$  which results in a smooth potential.

Based on numerical tests we developed the following procedure for choosing  $\lambda$ : First, we perform a calculation using  $\lambda=0$  to determine the minimal error in the reconstructed electron density, measured as

$$\Delta_{\text{abs}} = \int |\rho_{\text{in}}(\mathbf{r}) - \rho_{\text{rec}}(\mathbf{r})|^2 d^3r, \quad (14)$$

that can be achieved for a given norm of the gradient. Next, we start with a rather large value of  $\lambda$  (usually  $10^{-3}$ ) and then successively decrease  $\lambda$  until the error in the reconstructed electron density is smaller than 1.2 times the error when applying  $\lambda=0$ . While this procedure is less rigorous than the L-curve analysis described in Ref. 63, it turns out to yield potentials of similar quality and is much simpler to automate. The quality of the resulting potentials is assessed in more detail in Sec. IV.

### C. Choice of the frozen density

In principle, for a given  $\rho_2(\mathbf{r})$ , FDE with the exact  $v_T[\rho_1, \rho_2](\mathbf{r})$  yields the correct  $\rho_1$  density, i.e., one obtains  $\rho_1$  such that  $\rho_{\text{tot}} = \rho_1 + \rho_2$  is equal to the electron density that is obtained in a KS-DFT calculation on the full system. However, this can only be achieved if the frozen  $\rho_2(\mathbf{r})$  is chosen such that the exact  $\rho_1(\mathbf{r}) = \rho_{\text{tot}}(\mathbf{r}) - \rho_2(\mathbf{r})$  fulfills certain conditions.<sup>16</sup> First,  $\rho_1(\mathbf{r})$  must be non-negative everywhere in space, i.e.,  $\rho_2(\mathbf{r}) \leq \rho_{\text{tot}}(\mathbf{r})$ . Otherwise, the required  $\rho_1$  would be negative in certain regions, which is not possible to achieve. Furthermore,  $\rho_1$  needs to be a  $v_s$ -representable electron density, meaning that it must be possible to obtain this electron density as the ground state of a Kohn–Sham potential. This is not the case if, for instance, the required  $\rho_1(\mathbf{r})$  density has nodes (i.e., surfaces where the density is zero). In this situation, the potential would have to be singular [ $v(\mathbf{r}) = \infty$ ] at these nodes. [Note, however, that even though such densities can in principle be  $v_s$ -representable (see, e.g., Appendix A of Ref. 69), the required singular potentials are very difficult to represent in practical calculations, so that at least “in practice” such densities with nodes are not  $v_s$ -representable.] Usually these two conditions are not fulfilled for common choices of  $\rho_2(\mathbf{r})$ .

For calculating accurate reference potentials for  $v_T(\mathbf{r})$ , it is therefore of crucial importance to find a suitable partitioning of the total electron density into subsystem electron densities. In practical applications of FDE, one usually starts with an approximate  $\rho_2(\mathbf{r})$  which is obtained by performing a calculation on the isolated subsystem 2. However, in this case the condition that  $\rho_2(\mathbf{r}) \leq \rho_{\text{tot}}(\mathbf{r})$  is, in general, not fulfilled<sup>41</sup> because the exact  $\rho_2(\mathbf{r})$  density is too small in some regions in space and too large in other regions. For the purpose of this work, we want to avoid this problem by explicitly constructing  $\rho_2(\mathbf{r})$ , such that  $\rho_2(\mathbf{r}) \leq \rho_{\text{tot}}(\mathbf{r})$  everywhere. Therefore, we chose to construct the subsystem electron densities from localized molecular orbitals obtained in the KS-DFT calculation on the full system. From these localized molecular orbitals, those centered on subsystem 2 are chosen, and  $\rho_2(\mathbf{r})$  is obtained as

$$\rho_2(\mathbf{r}) = \sum_{i \in \text{subsystem2}} |\phi_i^{\text{LMO}}(\mathbf{r})|^2. \quad (15)$$

However, also this choice of  $\rho_2(\mathbf{r})$  turns out to be not without problems. The localized molecular orbitals of the supermolecular system are not perfectly localized to one of the sub-

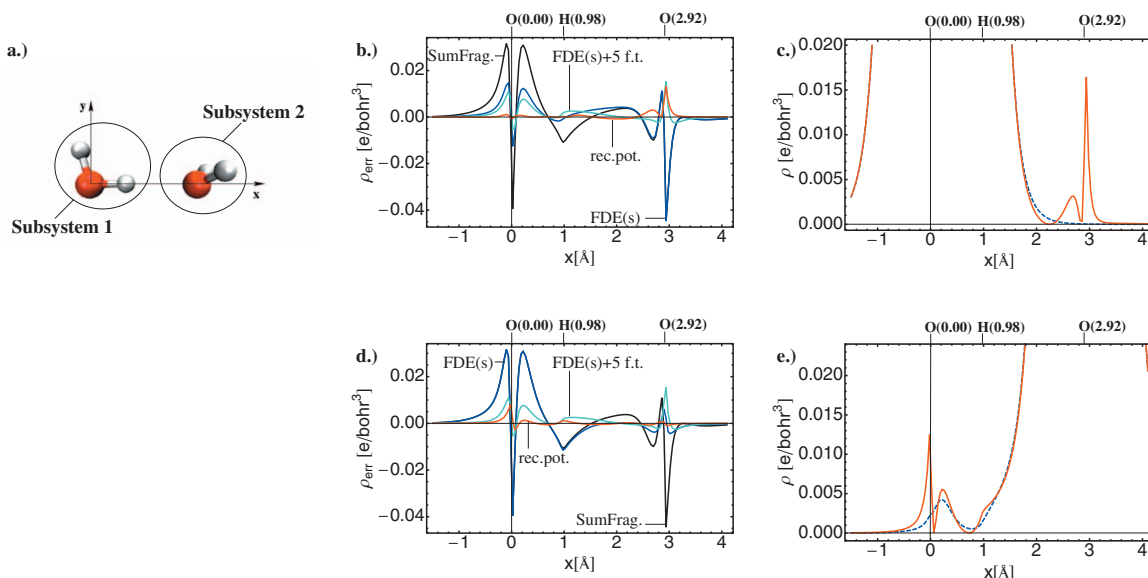


FIG. 1. (a) BP86/QZ4P optimized structure of a water dimer. [(b) and (d)] Difference densities with respect to supermolecular KS-DFT calculation for electron density obtained from the potential reconstruction (rec.pot., red line), the sum of the densities of the isolated fragments (SumFrag, black line), the density from a FDE(s) calculation [FDE(s), blue line], and the density from a FDE(s) employing five freeze-and-thaw cycles [FDE(s)+5 f.t., cyan line] for the water dimer. [(c) and (e)] Comparison of the reference electron density (red solid line) and the one obtained from the potential reconstruction (blue dashed line) for the water dimer. In (b) and (c) subsystem 1 is the active subsystem, while in (d) and (e) subsystem 2 is active.

systems and have tails that extend to atoms of the other subsystem. Furthermore, because of the orthogonality requirements, they show nodes at these atoms, which also leads to tails in the corresponding electron density. Therefore, the  $\rho_1(\mathbf{r})$  density is, in general, not  $v_s$ -representable, and the reconstruction of the potential will thus not be able to exactly yield the target  $\rho_1(\mathbf{r})$  density, but instead a reconstructed potential is obtained that results in the “best possible” density.

#### D. Computational details

All calculations were carried out using the FDE implementation<sup>14,17</sup> in the Amsterdam density functional package ADF.<sup>70</sup> For the potential reconstruction, a locally modified version of ADF has been used together with PYADF,<sup>71</sup> a scripting framework for quantum chemistry. If not stated otherwise, the potential obtained from a calculation of the isolated subsystem was used as initial guess  $v_0(\mathbf{r})$ . All molecular structures were optimized with the BP86 exchange-correlation functional<sup>72,73</sup> in combination with the QZ4P basis set of the ADF basis set library.<sup>70</sup> Localized orbitals were obtained using the Boys localization criterion<sup>74–76</sup> as implemented in ADF. In all FDE calculations, the supermolecular basis set expansion,<sup>36</sup> in which the basis functions of both subsystems are employed to expand the subsystem electron densities, was used. Later, the use of the supermolecular basis set expansion will be denoted as FDE(s).

In the embedding calculations, two different kinetic-energy functionals have been applied to approximate the kinetic-energy component of the effective embedding potential. First, the TF LDA kinetic-energy density functional and, second, the PW91k GGA kinetic-energy density functional, which has the same functional form for the enhancement factor as the exchange functional of Perdew and Wang,<sup>77</sup> but

which has been reparametrized for the kinetic energy by Lembarki and Chermette.<sup>37</sup> The use of the PW91k functional to approximate  $v_T[\rho_1, \rho_2](\mathbf{r})$  was introduced in Ref. 35 and is therefore sometimes referred to as “GGA97 approximation” in the context of FDE calculations. For the visualization of the potentials, MATHEMATICA<sup>78</sup> was employed.

### III. ACCURACY OF THE RECONSTRUCTED ELECTRON DENSITY

Before we proceed to the calculation of accurate embedding potentials, we validate our methodology by investigating how accurately the reference  $\rho_1(\mathbf{r})$  electron density obtained from localized molecular orbitals can be reconstructed. We carried out calculations on different model systems consisting of subsystems which are connected by bonds varying from a rather weak hydrogen bond to a strong covalent bond.

As a first model system, we considered a water dimer, which is divided into two subsystems each containing one single water molecule. These two subsystems are connected by a hydrogen bond. Hence, it is a good example for a system which exhibits only weak interactions between the subsystems, and since FDE has been successfully applied to such systems, one would expect the errors in the approximation to  $v_T[\rho_1, \rho_2](\mathbf{r})$  to be small. The optimized structure is shown in Fig. 1(a). In this dimer structure, there is a hydrogen bond between a hydrogen atom of the first water molecule (subsystem 1, shown on the left) and the oxygen atom of the second water molecule (subsystem 2, shown on the right). The molecule is oriented such that this hydrogen bond is aligned on the  $x$ -axis, with the oxygen atom defining the origin of the coordinate system.

First, we consider the case in which subsystem 1 is active and subsystem 2 is frozen. In this case, the electron pair

TABLE I. Absolute error  $\Delta^{\text{abs}}$  (in units of the elementary charge) with respect to a supermolecular KS-DFT calculation for the sum of the densities of the isolated fragments (SumFrag), for FDE(s), with and without five freeze-and-thaw cycles, and for the density obtained from the reconstructed potential (rec.pot.)

	Active subsystem	SumFrag	FDE(s)	FDE(s)+5 f.t.	rec.pot.
H <sub>2</sub> O–H <sub>2</sub> O	First H <sub>2</sub> O	0.1528	0.1048	0.0332	0.0178
H <sub>2</sub> O–H <sub>2</sub> O	Second H <sub>2</sub> O		0.1136		0.0108
F–H–F <sup>-</sup>	F–H	0.8280	0.5858	0.1196	0.0544
F–H–F <sup>-</sup>	F <sup>-</sup>		0.7200		0.0477
BH <sub>3</sub> NH <sub>3</sub>	BH <sub>3</sub>	0.9170	0.7673	0.6306	0.0773
BH <sub>3</sub> NH <sub>3</sub>	NH <sub>3</sub>		0.6295		0.0979
C <sub>2</sub> H <sub>6</sub>	CH <sub>3</sub> <sup>+</sup>	1.9061	1.7283	2.9773	0.0900
C <sub>2</sub> H <sub>6</sub>	CH <sub>3</sub> <sup>-</sup>		1.2960		0.1815

forming the hydrogen bond is contained in the frozen subsystem. Along this  $x$ -axis, Fig. 1(b) shows the difference,

$$\rho_{\text{err}}^{\text{rec}}(\mathbf{r}) = \rho_1^{\text{ref}}(\mathbf{r}) - \rho_1^{\text{rec}}(\mathbf{r}) = \rho_{\text{tot}}(\mathbf{r}) - (\rho_1^{\text{rec}}(\mathbf{r}) + \rho_2(\mathbf{r})), \quad (16)$$

between the reference electron density  $\rho_1^{\text{ref}}(\mathbf{r}) = \rho_{\text{tot}}(\mathbf{r}) - \rho_2(\mathbf{r})$  and the electron density  $\rho_1^{\text{rec}}(\mathbf{r})$  (red line) obtained from the reconstructed potential, where  $\rho_1^{\text{ref}}(\mathbf{r})$  and  $\rho_2(\mathbf{r})$  have been obtained from localized molecular orbitals as described above. Overall, this difference is rather small. The only significant deviation from zero corresponds to two peaks which are located close to the oxygen atom of the frozen subsystem.

In order to put these errors in perspective, we compare them to the errors in the electron density one obtains if the sum of the electron densities of the isolated subsystems (SumFrag), the electron density from a FDE(s) calculation, or from a FDE calculation in which  $\rho_2(\mathbf{r})$  is updated in five freeze-and-thaw (f.t.) cycles is used. In these approximate FDE calculations, the PW91k kinetic-energy functional has been used to approximate  $v_{\text{T}}$ . The difference densities,

$$\rho_{\text{err}}^{\text{FDE}}(\mathbf{r}) = \rho_{\text{tot}} - (\rho_1^{\text{FDE}}(\mathbf{r}) + \rho_2^{\text{(FDE)}}(\mathbf{r})), \quad (17)$$

for the sum of the isolated fragments (black line), FDE(s) (blue line), and FDE(s)+5 f.t. (cyan line) are also included in Fig. 1(b). The comparison shows that for the reconstructed potential, the difference is significantly smaller than for approximate FDE. Of course, the largest error is observed for the sum of the isolated fragments because in this case the interaction between the two water molecules is neglected entirely. For FDE(s) without freeze-and-thaw cycles, the quality of the resulting electron density has improved in the region of the active subsystem. However, since the density of the other subsystem is frozen, the errors at this subsystem remain unchanged. If both subsystem electron densities are updated in freeze-and-thaw cycles, the difference is also decreasing at the frozen subsystem and in between both subsystems.

To quantify these errors, the integral of the absolute value of the difference densities<sup>47,48,79</sup> (referred to as *absolute errors* in the following),  $\Delta^{\text{abs}} = \int |\rho_{\text{err}}(\mathbf{r})| d^3r$ , are given in Table I. When applying the reconstructed potential the error in the electron density is approximately one order of magnitude smaller than for the sum of the fragment electron densities, about six times smaller than for FDE(s), and half of the error when comparing to FDE(s) with freeze-and-thaw

cycles. It is important to note that for practical applications the errors of the FDE(s) calculations with the approximate PW91k functional are acceptably small, as it is shown by the successful application of FDE for such hydrogen-bonded systems.

The same calculations were also performed for subsystem 2 as active subsystem, with subsystem 1 being frozen. In this case, the active subsystem comprises the oxygen lone pair which engages in the hydrogen bond between the subsystems. The difference densities are shown in Fig. 1(d). This error in the reconstructed density is somewhat smaller than for the calculations where subsystem 1 is active, and significantly smaller than in the approximate FDE calculations. This is also confirmed by the absolute errors given in Table I.

The second model system is the fluoride adduct of hydrofluoric acid F–H–F<sup>-</sup> which contains two equivalent F–H bonds. The optimized structure of F–H–F<sup>-</sup> is shown in Fig. 2(a). We divided this molecule into two asymmetric fragments, one containing a neutral hydrofluoric acid unit (subsystem 1, shown on the left) and the other one consisting of a fluoride anion (subsystem 2, shown on the right). The molecule is oriented such that the fluorine atom of subsystem 1 is located at the origin of the coordinate system and that all atoms lie on the  $x$ -axis. This molecule is a challenging situation for FDE because one has to recover a symmetric electron density starting from asymmetric fragments.<sup>41</sup> F–H–F<sup>-</sup> has already been the subject of a FDE study,<sup>41</sup> in which Kiewisch *et al.* compared the electron density obtained from embedding calculations with the electron density of a KS-DFT calculation on the full system by means of a topological analysis. It was shown that despite the strong hydrogen bond, a qualitatively correct description of the electron density of F–H–F<sup>-</sup> can be achieved.

For the case where F–H is the active subsystem (i.e., the electron pair engaged in the hydrogen bond is not included in the active subsystem), the difference densities  $\rho_{\text{err}}^{\text{rec}}$  and  $\rho_{\text{err}}^{\text{FDE}}$  are shown in Fig. 2(b). The difference in the electron density resulting from the reconstructed potential is almost as small as for the water dimer. The major part of the difference is concentrated in three peaks which are located around the two fluorine nuclei. These peaks are higher than for the water dimer, but when these errors are put in relation to those obtained from approximate FDE calculations, they are still rather small (see also the absolute errors listed in Table I).

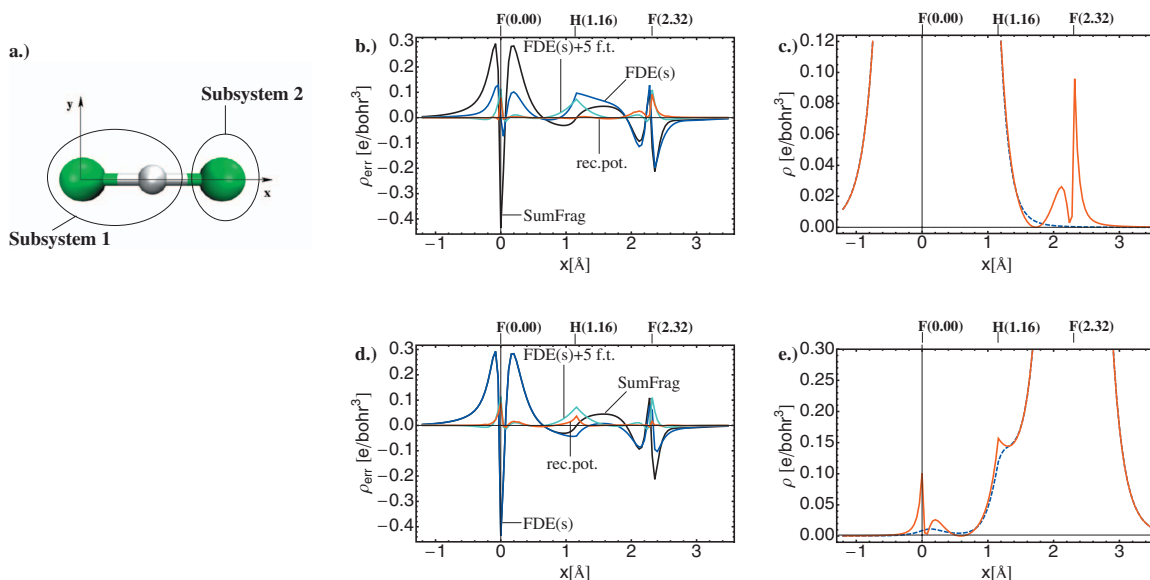


FIG. 2. (a) BP86/QZ4P optimized structure of F–H–F<sup>-</sup>. [(b) and (d)] Difference densities with respect to supermolecular KS-DFT calculation for electron density obtained from the potential reconstruction (rec.pot., red line), the sum of the densities of the isolated fragments (SumFrag, black line), the density from a FDE(s) calculation [FDE(s), blue line], and the density from a FDE(s) employing five freeze-and-thaw cycles [FDE(s)+5 f.t., cyan line] for F–H–F<sup>-</sup>. [(c) and (e)] Comparison of the reference electron density (red solid line) and the one obtained from the potential reconstruction (blue dashed line) for F–H–F<sup>-</sup>. In (b) and (c) subsystem 1 (F–H) is the active subsystem, while in (d) and (e) subsystem 2 (F<sup>-</sup>) is active.

However, as shown in Ref. 41 errors of this size are still acceptable for most practical applications. Again, the absolute error for the reconstructed electron density is about half the error of the best approximate FDE calculation. For the F<sup>-</sup> anion as the active subsystem, the difference densities are shown in Fig. 2(d). Similar to the case where F–H is active, the error in the reconstructed density is rather small (see also Table I) and by approximately a factor of 2 smaller than the error of approximate FDE calculations including freeze-and-thaw cycles.

As a third model system featuring a donor–acceptor

bond, ammonia borane BH<sub>3</sub>NH<sub>3</sub> [see Fig. 3(a) for the optimized structure] is considered, which is divided into a BH<sub>3</sub> molecule (subsystem 1, shown on the left) and a NH<sub>3</sub> molecule (subsystem 2, shown on the right). The molecule is oriented such that the boron atom is located at the origin of the coordinate system and the nitrogen atom is lying on the  $x$ -axis. Although the donor–acceptor bond connecting both subsystems is weaker than the hydrogen bond in F–H–F<sup>-</sup>, it can be expected that the error in the embedding electron density for ammonia borane is larger due to the larger covalent character of such a coordination bond. In an earlier

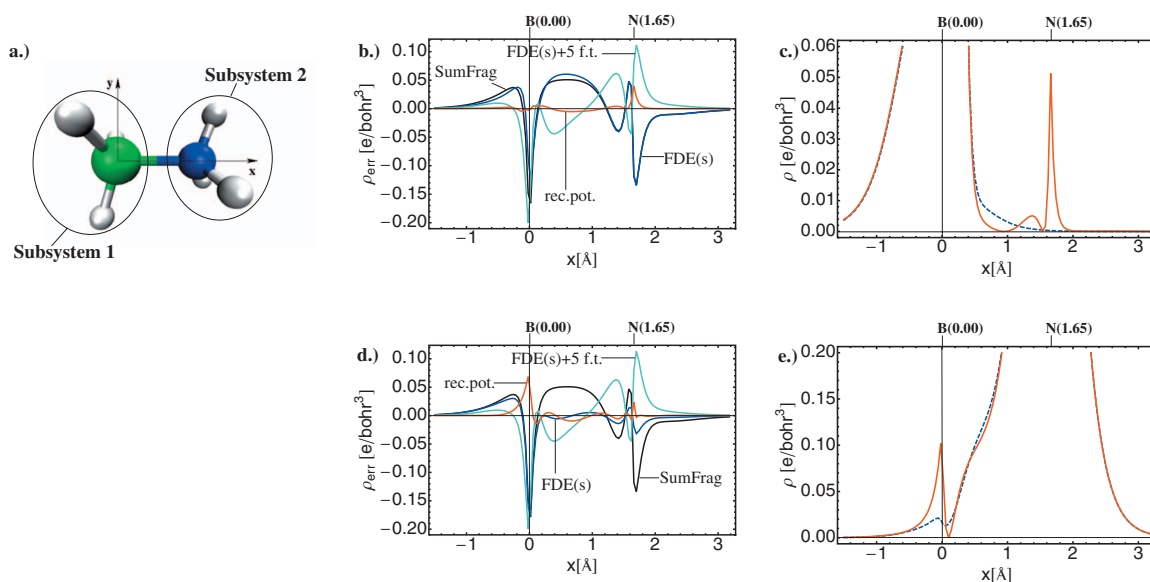


FIG. 3. (a) BP86/QZ4P optimized structure of ammonia borane. [(b) and (d)] Difference densities with respect to supermolecular KS-DFT calculation for electron density obtained from the potential reconstruction (rec.pot., red line), the sum of the densities of the isolated fragments (SumFrag, black line), the density from a FDE(s) calculation [FDE(s), blue line], and the density from a FDE(s) employing five freeze-and-thaw cycles [FDE(s)+5 f.t., cyan line] for ammonia borane. [(c) and (e)] Comparison of the reference electron density (red solid line) and the one obtained from the potential reconstruction (blue dashed line) for ammonia borane. In (b) and (c) subsystem 1 (BH<sub>3</sub>) is the active subsystem, while in (d) and (e) subsystem 2 (NH<sub>3</sub>) is active.

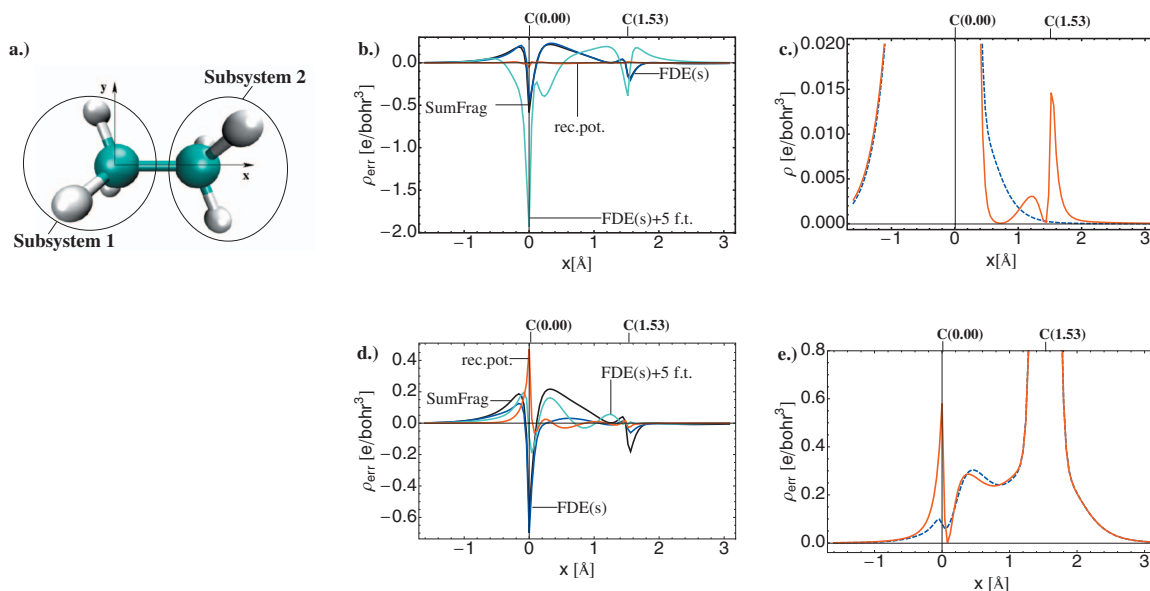


FIG. 4. (a) BP86/QZ4P optimized structure of ethane. [(b) and (d)] Difference densities with respect to supermolecular KS-DFT calculation for electron density obtained from the potential reconstruction (rec.pot., red line), the sum of the densities of the isolated fragments (SumFrag, black line), the density from a FDE(s) calculation [FDE(s), blue line], and the density from a FDE(s) employing five freeze-and-thaw cycles [FDE(s)+5 f.t., cyan line] for ethane. [(c) and (e)] Comparison of the reference electron density (red solid line) and the one obtained from the potential reconstruction (blue dashed line) for ethane. In (b) and (c) subsystem 1 ( $\text{CH}_3^+$ ) is the active subsystem, while in (d) and (e) subsystem 2 ( $\text{CH}_3^-$ ) is active.

study,<sup>46</sup> the electron density distribution of ammonia borane obtained from FDE calculations was analyzed using a topological analysis. It was found that FDE works qualitatively correctly but the resulting electron density exhibits larger deficiencies in the bonding region. The topological analysis of the electron density resulted in the wrong sign for the negative Laplacian (which at the bond critical point of the B–N coordination bond is an indicator for the type of bond under investigation<sup>80</sup>).

First, we turn to the case where  $\text{BH}_3$  is the active subsystem. The difference electron densities with respect to the supermolecular KS-DFT calculation are shown in Fig. 3(b). Again,  $\rho_{\text{err}}^{\text{rec}}(\mathbf{r})$  is, in general, very small. It is large at two peaks at the position of the nitrogen atom of the frozen subsystem. These errors can be compared to electron densities obtained from approximate FDE calculations. The two curves for the sum of the fragment electron densities and FDE(s) are almost identical, i.e., FDE(s) does not improve substantially over a simple sum of fragments density. If the frozen density is updated in freeze-and-thaw cycles, the difference density changes, but large errors still remain. This observation is reinforced by the absolute errors shown in Table I. For the sum of fragments as well as for the approximate FDE calculations, the absolute errors are comparable. It is thus not possible to obtain a correct description for ammonia borane with standard FDE calculations using the approximate PW91k kinetic-energy functional. Applying the reconstructed potential instead leads to errors which are significantly smaller than those of approximate FDE calculations, even though they are larger than for the water dimer and  $\text{F–H–F}^-$ . For  $\text{NH}_3$  (subsystem 2) as the active subsystem, the difference densities are shown in Fig. 3(d). In this case the active subsystem contains the lone pair of  $\text{NH}_3$ , which forms the coordination bond between the subsystems. The error in the reconstructed density is slightly larger than

for the calculations where  $\text{BH}_3$  is active, but it is still almost an order of magnitude smaller than those found in approximate FDE calculations.

As a last model system, we consider ethane for which the optimized structure is shown in Fig. 4(a). It is partitioned into a positively charged  $\text{CH}_3^+$  (subsystem 1, shown on the left) and a negatively charged  $\text{CH}_3^-$  fragment (subsystem 2, shown on the right). The molecule is oriented such that the covalent bond between the carbon atoms lies on the  $x$ -axis, with the carbon atom of subsystem 1 defining the origin of the coordinate system. As for  $\text{F–H–F}^-$ , we start from two asymmetric fragments, trying to obtain a symmetric electron density as a final result of the embedding procedure. Both subsystems are connected by a covalent bond, which presents a challenge for FDE. Because the common approximations used for  $v_{\text{T}}[\rho_1, \rho_2]$  break down in such situations for any available approximate kinetic-energy density functional, it is not possible to obtain a reasonable description for the electron density from approximate FDE calculation.

This failure is obvious from the difference densities  $\rho_{\text{err}}^{\text{FDE}}$  shown in Fig. 4(b), where we first consider the case in which  $\text{CH}_3^+$  is the active subsystem. Already the error for the sum of isolated fragments is huge, as can also be seen from the absolute error amounting to nearly two elementary charges (see Table I). This situation does not improve significantly in the FDE(s) calculations, and when applying freeze-and-thaw cycles, the error increases further. For such strongly interacting subsystems, the freeze-and-thaw cycles do not converge and impair the quality of the electron density.<sup>42</sup> In contrast, the error obtained when applying the reconstructed potential is acceptably small, as can be seen from the inspection of  $\rho_{\text{err}}^{\text{rec}}$  in Fig. 4(b). As the absolute error listed in Table I shows, the error of the reconstructed density is comparable to the one found for ammonia borane. The results for the calculations where subsystem 2 ( $\text{CH}_3^-$ ) is active are presented in Fig. 4(d).

In this case the active subsystem contains the electron pair forming the covalent bond, and the absolute error in the reconstructed density is about twice as large as for  $\text{CH}_3^+$  as the active subsystem. Even though the absolute error is somewhat larger, it is still comparable to the error for FDE(s) +5 f.t. for  $\text{F-H-F}^-$ , which still lies within the acceptable range.

Summarizing these results, in all cases the potential reconstruction yields rather accurate electron densities. For the weakly bonded water dimer, the absolute error in the reconstructed electron density is about half the error obtained in an approximate FDE calculation, while for the strong covalent bond in ethane, the absolute error of the reconstructed electron density is still comparable to the one obtained with FDE(s) for the water dimer. The reconstructed electron density is always significantly more accurate than the densities obtained in approximate FDE calculations. This is particularly true for the systems that are difficult for approximate FDE, i.e., those where the subsystems are connected by a coordination bond or by a covalent bond.

To understand the origin of the remaining small error in the reconstructed electron density, Fig. 1(c) shows the reference electron density  $\rho_1^{\text{ref}}(\mathbf{r})$ , obtained from localized molecular orbitals of the full system, compared to the reconstructed electron density  $\rho_1^{\text{rec}}(\mathbf{r})$  for subsystem 1 of the water dimer. The figure focuses on the region where the largest part of the differences originates. Due to the orthogonality constraint of the localized molecular orbitals of the total system, the reference electron density contains one node (i.e., a surface where the electron density is zero) at the position of the oxygen atom of the frozen subsystem. A second node is found between the two subsystems at about 2.2 Å. As discussed above in Sec. II C, such an electron density is (at least in practice) not  $v_s$ -representable, i.e., no potential exists that can reproduce it exactly. Hence, these tails in the electron density cannot be captured by the potential reconstruction algorithm. Because the reconstructed electron density is too small close to the oxygen atom, it has to be too large somewhere else, and therefore a slightly too large reconstructed electron density is found in the region between the two subsystems. For subsystem 2 of the water dimer, the reference and the reconstructed density are compared in Fig. 1(e). Again, the reference density has two nodes, one close to the hydrogen atom and one close to the oxygen atom and is, therefore, not  $v_s$ -representable. Hence, the potential reconstruction can only result in an approximation to it. Instead of reproducing two peaks at the frozen oxygen, which are caused by the tails of the localized orbitals, only a single peak that reproduces part of the reference density is obtained. Note that this is different from the case of subsystem 1 being active shown in Fig. 1(d), where the small peaks in the reference density at the frozen oxygen atom are not captured by the reconstruction at all.

For the other model systems, the origin of the error in the reconstructed electron density is similar. For  $\text{F-H-F}^-$ , ammonia borane, and ethane the reference and the reconstructed electron densities for both subsystems are depicted in Figs. 2(c) and 2(e), 3(c) and 3(e), and in Figs. 4(c) and 4(e), respectively. In all cases the reference electron density

exhibits nodes and is thus not  $v_s$ -representability, i.e., the errors observed in the reconstructed electron densities are caused by our choice of the reference density, which we construct from localized molecular orbitals. Because of the nodes in the reference density, some features of the reference density behind these nodes cannot or only partly be captured in the reconstruction of the potential. The stronger the interaction between the subsystems is, the larger is the amount of electron density behind these nodes, leading to a larger error in the reconstructed electron density.

#### IV. ACCURACY OF RECONSTRUCTED POTENTIALS

Next, we assess the accuracy of the reconstructed potentials themselves. This is not possible from the calculations discussed so far because in these calculations the correct KS potential is not known. Therefore, we performed the potential reconstruction for the electron densities of systems where the KS potential from which these densities were obtained is available.

We start with an isolated water molecule and employ the structure of the first water molecule (subsystem 1) of the water dimer considered above. For the electron density calculated in a KS-DFT calculation for this water molecule, we perform a potential reconstruction in which we start from the KS potential  $v_0(\mathbf{r})$  that ADF uses as initial guess in the first self-consistent field iteration, the KS potential calculated from the superposition of atomic densities. The reconstruction should reproduce the difference between this initial and the fully self-consistent KS potentials of the isolated water molecule. The reconstructed part of the KS potential [i.e.,  $v_{\text{rec}}(\mathbf{r}) - v_0(\mathbf{r})$ ] are shown in Fig. 5(a). Both the reconstructed potential obtained without applying the smoothing constraint, i.e., for  $\lambda=0$  (blue dashed line), as well as the one obtained with smoothing constraint (red dashed line) are shown. In the latter case, the optimal  $\lambda$  is chosen as explained in Sec. II B. Both reconstructed potentials are almost identical.

The reconstructed potential can be compared to  $v_{\text{KS}}(\mathbf{r}) - v_0(\mathbf{r})$  [solid black line in Fig. 5(a)], where  $v_{\text{KS}}(\mathbf{r})$  is the KS potential from the calculations on the isolated water molecule. Because the reconstructed potential is only defined up to a constant, the reconstructed potentials are shifted such that they agree best with the correct potential, i.e., such that  $\int \rho(\mathbf{r})(v_{\text{rec}}(\mathbf{r}) - v_{\text{KS}}(\mathbf{r}))d^3r$  is minimal. As the figure shows, the reconstructed potential agrees very well with the KS potential from which the reference density was obtained.

As a second test, we consider the  $\text{F-H}$  molecule (i.e., the isolated subsystem 1 of  $\text{F-H-F}^-$ ). Again, we performed a potential reconstruction for the reference density from a KS-DFT calculation for the isolated molecule, in which the initial potential was obtained for a superposition of atomic densities. The KS potential from which the reference density was obtained as well as the reconstructed potentials (all minus the initial potential  $v_0$ ) are shown in Fig. 5(b). When the potential reconstruction is performed without the smoothing constraint (i.e., for  $\lambda=0$ ), the reconstructed potential deviates significantly from the correct KS potential. However, with

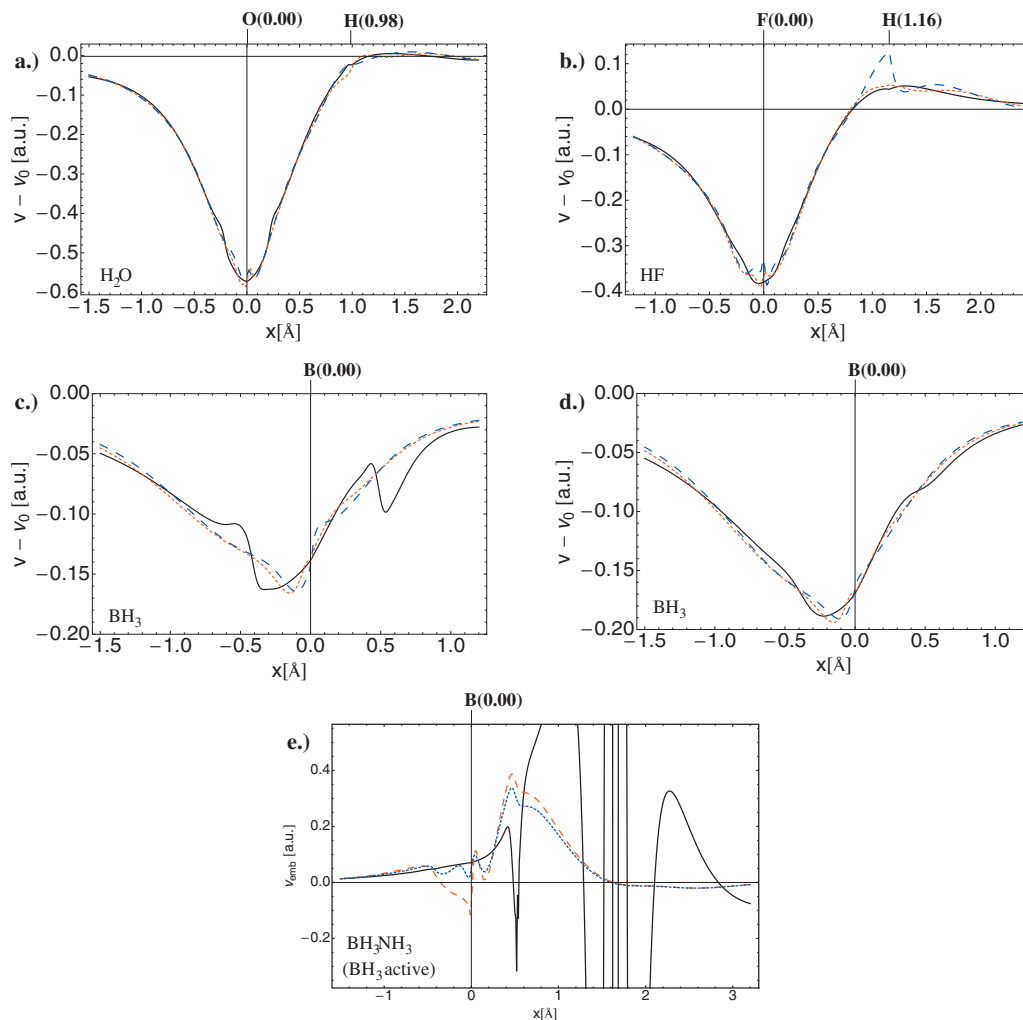


FIG. 5. Reconstructed potentials obtained with (red dashed line) and without additional smoothing constraint (blue dashed line) compared to the KS potential from which the reference density was obtained (black solid line). The initial guess for the potential was subtracted from all potentials in order to better visualize the differences. (a) Isolated  $\text{H}_2\text{O}$  molecule, (b) isolated F–H molecule, (c) isolated  $\text{BH}_3$  molecule using BP86, (d) isolated  $\text{BH}_3$  molecule using LDA, and (e)  $\text{BH}_3$  subsystem of ammonia borane.

smoothing constraint and with the optimal  $\lambda$  chosen as described above, a very good agreement is obtained.

For the  $\text{BH}_3$  molecule (i.e., the isolated subsystem 1 of ammonia borane), the reconstructed potential as well as the KS potential from which the reference density has been obtained are shown in Fig. 5(c) (from all potentials the initial potential  $v_0$  has been subtracted). The reference potential shows oscillatory features at about  $0.5 \text{ \AA}$  as well as at about  $-0.5 \text{ \AA}$ . These features are not reproduced by the reconstructed potential. Instead, a smooth potential is obtained that averages over these features of the reference KS potential. Nevertheless, within the chosen convergence thresholds, the same electron density is obtained from this reconstructed potential, i.e., a smoother potential yielding the same density is obtained from the reconstruction. The oscillations in the reference KS potential originate from the BP86 exchange–correlation potential. If the LDA exchange–correlation potential is employed [see Fig. 5(d)], the oscillations disappear and the reconstructed potential agrees well with the reference KS potential.

Finally, we performed a potential reconstruction in which the density of the active  $\text{BH}_3$  subsystem from an approximate FDE calculation for ammonia borane is used as reference. As initial potential  $v_0$  in the potential reconstruction, the KS potential of an isolated  $\text{BH}_3$  molecule was used. The reconstructed potential is shown in Fig. 5(e) along with the KS potential from which the reference density has been obtained. This reference potential now includes the embedding potential, which is highly oscillatory around the nitrogen atom of the frozen subsystem. These oscillations are not captured in the reconstructed potential, and instead a smooth potential is obtained. Note again that this smoother potential leads to the same electron density, i.e., the oscillations in the embedding potential are not reflected in the electron density, even though basis functions on the frozen subsystem have been included in the calculation. The fact that such oscillations in the potential only slightly affect the electron density is one of the reasons for the problems experienced when reconstructing potentials from electron densities as well as for those observed in optimized effective potential methods.<sup>63–68</sup>

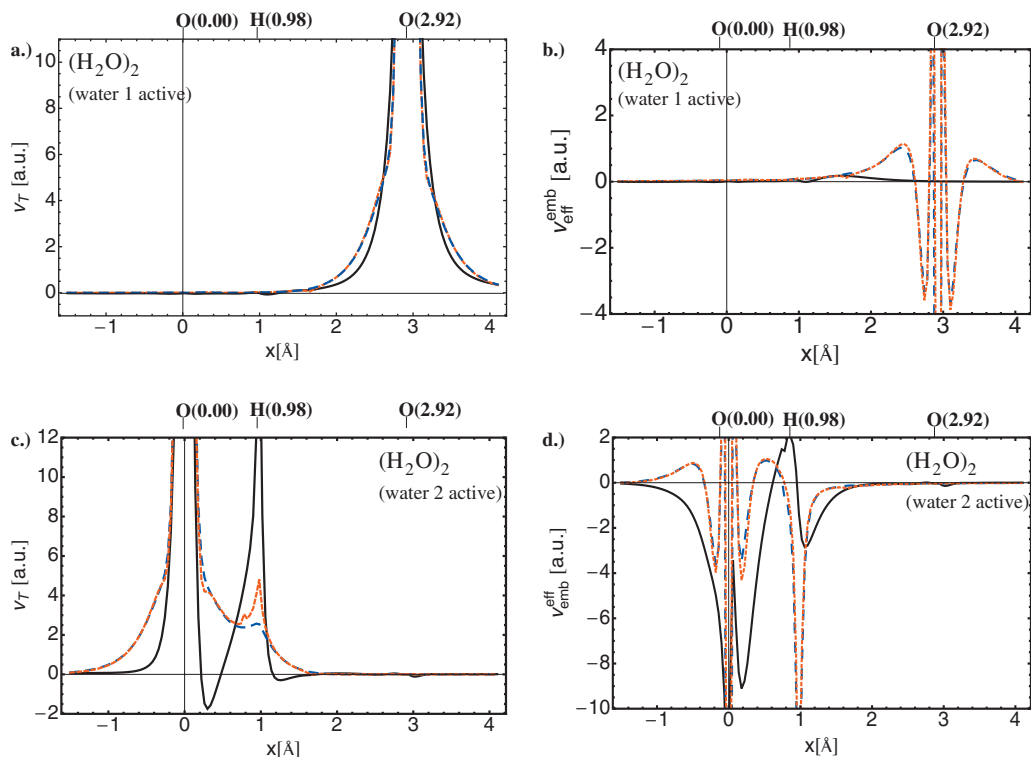


FIG. 6. Comparison of (a) the accurate kinetic-energy component  $v_T(r)$  and (b) the total embedding potentials  $v_{\text{emb}}^{\text{eff}}(r)$  (both black solid line) with approximate potentials obtained using the TF (blue dashed line) and PW91k (red dashed line) functionals for a water dimer with active subsystem 1. [(c) and (d)] Comparison of accurate and approximate potentials for active subsystem 2.

Overall, our investigations show that the implemented algorithm yields smooth and physically meaningful reconstructed potentials. However, not in all cases is the reconstructed potential identical to the one from which the reference density has been obtained. If this reference potential shows oscillations, it is possible that a smoother reconstructed potential is obtained. Still, this “simpler” potential yields the same electron density, i.e., from the potential reconstruction one obtains the smoothest possible potential even though the orbital energies, in particular, of virtual orbitals, might differ. Of course, in the basis set limit the potential reconstruction should result in a unique potential. Note, however, that in a finite basis set also the KS potential is ambiguous. For the KS potential from which the reference density is obtained in a finite basis set, in general, a different density would result in the basis set limit.

## V. ACCURATE EMBEDDING POTENTIALS

After the discussion of the quality of the electron densities and of the potentials obtained from the reconstruction algorithm in the previous sections, we have now all tools available that are required for calculating accurate reference potentials for  $v_T[\rho_1, \rho_2]$ . These will be compared to approximate potentials derived from the TF and the PW91k kinetic-energy functionals. For an analysis of the errors in these approximate potentials, we compare both the kinetic-energy component  $v_T$  itself and the total effective embedding potential  $v_{\text{emb}}^{\text{eff}}$  of Eq. (1). Since differences between the accurate reference and approximate potentials only occur in the kinetic-energy component, the same differences will be ob-

served in both cases. However, due to the large repulsive part of  $v_T$ , which has to compensate the strongly attractive nuclear potential contribution of the effective embedding potential, the absolute value of the total embedding potential, in general, much smaller so that errors are easier to identify when comparing  $v_{\text{emb}}^{\text{eff}}$ . The potentials are compared for the model systems described in Sec. III, where for each model system we discuss the potentials for each of the subsystems being active.

### A. Water dimer

We start again with the water dimer and first consider subsystem 1 as active subsystem. In this case the electron pair forming the hydrogen bond is included in the frozen subsystem. Both the accurate and the approximate results for  $v_T[\rho_1, \rho_2]$  obtained for the water dimer are presented in Fig. 6(a). The accurate reference potential (solid black line) is almost zero at the active subsystem. At the frozen subsystem it is strongly repulsive because it has to compensate the attractive nuclear potential of the nuclei in the frozen subsystem. From the accurate reference for the total embedding potential  $v_{\text{emb}}^{\text{eff}}(r)$  shown in Fig. 6(b) (solid black line), it is obvious that the kinetic-energy component and the nuclear potential contribution cancel each other entirely with the consequence that  $v_{\text{emb}}^{\text{eff}}$  is zero at the frozen subsystem. This is in agreement with the results of Ref. 43, where it was shown that, in the long-distance limit of two subsystems at large separation and under the condition that the density at the frozen subsystem is close to the exact total density (i.e., there is no charge transfer between the subsystems), the embed-

ding potential at the frozen subsystem should be exactly zero. While for the water dimer considered here the distance between the subsystems is rather small so that the long-distance limit should not strictly apply, it turns out that the exact result obtained in the long-distance limit still holds very well. Only in between the two subsystems at approximately 0.8–1.6 Å the accurate embedding potential  $v_{\text{eff}}^{\text{emb}}(\mathbf{r})$  is different from zero and weakly repulsive.

The two considered approximate kinetic-energy functionals (blue and red dashed lines for TF and PW91k, respectively) yield very similar potentials for this model system and are therefore discussed together. The weakly repulsive embedding potential between the water molecules is fully recovered by both approximate functionals. However, when moving closer to the frozen subsystem the potential between 1.6 and 2.3 Å is overestimated by the approximate functionals, while closer to the oxygen nucleus of the frozen subsystem the embedding potential is overall attractive, with two narrow repulsive peaks occurring near the nucleus. Therefore, the approximate embedding potentials do not go to zero at 2.4 Å as the accurate reference potential does. This failure of the approximate TF and PW91k kinetic-energy functionals, i.e., their inability to compensate the large nuclear attraction, has already been pointed out and discussed in Ref. 43. While this failure seriously affects the energies of virtual KS orbitals and can thus lead to spurious low-lying excited states,<sup>43</sup> its effect on occupied orbitals and on the electron densities is usually only minor, in particular, if no basis functions extending on the frozen subsystem are included. For correctly reproducing the electron density of the active subsystem, it is more important that the embedding potential is accurate at the active subsystem and in between the two subsystems, where for the water dimer both the accurate reference and the approximate potentials are rather small or weakly repulsive.

For the second water molecule (subsystem 2) as active subsystem the kinetic energy component  $v_{\text{T}}$  and the embedding potential  $v_{\text{emb}}^{\text{eff}}$  are depicted in Figs. 6(c) and 6(d), respectively. The active subsystem now contains the oxygen lone pairs which form the hydrogen bond to the other water molecule. Therefore, both the kinetic energy component as well as the embedding potential itself show a more complicated structure than in the previous case. The accurate  $v_{\text{T}}$  features two repulsive peaks at the positions of the hydrogen and of the oxygen atoms of the frozen subsystem. However, in contrast to the case where the other water molecule is active, the kinetic energy does not exactly cancel the other components of the embedding potential anymore. Instead, the accurate embedding potential shown in Fig. 6(d) exhibits a weak repulsive maximum at the hydrogen atom while it is strongly attractive around the oxygen atom of the frozen subsystem with two distinct minima close to the oxygen atom. Because of the formation of the hydrogen bond, electron density of the nonfrozen water molecule subsystem extends to the frozen subsystem so that the assumptions made for deriving the exact embedding potential in the long-distance limit in Ref. 43 (i.e., that there is no charge transfer between

the subsystems) are no longer fulfilled. For this reason, the embedding potential at the frozen subsystem is no longer close to zero.

The potentials derived from the approximate TF and PW91k functionals are very similar, slight differences are only found close to the hydrogen atom. At the nonfrozen and in between the subsystem, the approximate embedding potentials are small and thus reproduce the accurate potential. At the hydrogen nucleus of the frozen subsystem, the approximate embedding potentials both show a rather sharp attractive peak. While at the hydrogen nucleus itself this does not agree with the accurate potential (which is repulsive), the attractive feature between the subsystems (close to the hydrogen nucleus) is at least partly reproduced. At the oxygen atom of the frozen subsystem, the approximate potentials are very similar to the one found above when the other water molecule is the active subsystem, i.e., the approximate potential is overall attractive, with two sharp repulsive peaks close to the oxygen atom. However, now the accurate reference is not zero, but is attractive itself. Therefore, the approximate potentials at least qualitatively capture the important features of the embedding potential, even though they are not attractive enough. Overall, despite the obvious shortcomings of the approximate potentials, the most important features of the embedding potential are captured correctly, in particular, the attractive potential in between the subsystems. This makes the good quality of the electron densities from approximate FDE calculations understandable.

## B. F–H–F<sup>-</sup>

For F–H–F<sup>-</sup>, we start by considering the situation where the F–H fragment (subsystem 1) is active (i.e., the electron pair forming the hydrogen bond is not included in the active subsystem), for which the accurate and approximate potentials are shown in Figs. 7(a) and 7(b). As for the water dimer, the accurate  $v_{\text{T}}$  is strongly repulsive at the frozen subsystem (here consisting of an anion) and compensates the nuclear attraction of the fluorine nucleus. Therefore, even for the strong hydrogen bond present in F–H–F<sup>-</sup>, the long-distance limit applies at the frozen subsystem. However, at the fluorine atom of the frozen subsystem, the approximate potentials are similar to those found above at the frozen oxygen atom for the water dimer. Therefore, the kinetic-energy component is not able to fully compensate the nuclear attraction which leads to an overall attractive embedding potential at the frozen subsystem. Between the two subsystems, the accurate embedding potential is repulsive in order to describe the redistribution of electron density due to the formation of the hydrogen bond. It is broader and significantly more repulsive than in the case of the water dimer, where the interaction and thus also the amount of density redistribution are smaller. Also at the nonfrozen subsystem, a slightly repulsive embedding potential is obtained.

The TF and PW91k kinetic-energy functionals lead to almost identical embedding potentials, which only differ slightly close to the hydrogen atom of the nonfrozen subsystem. They qualitatively reproduce the repulsive embedding potential between the subsystems, while they are almost

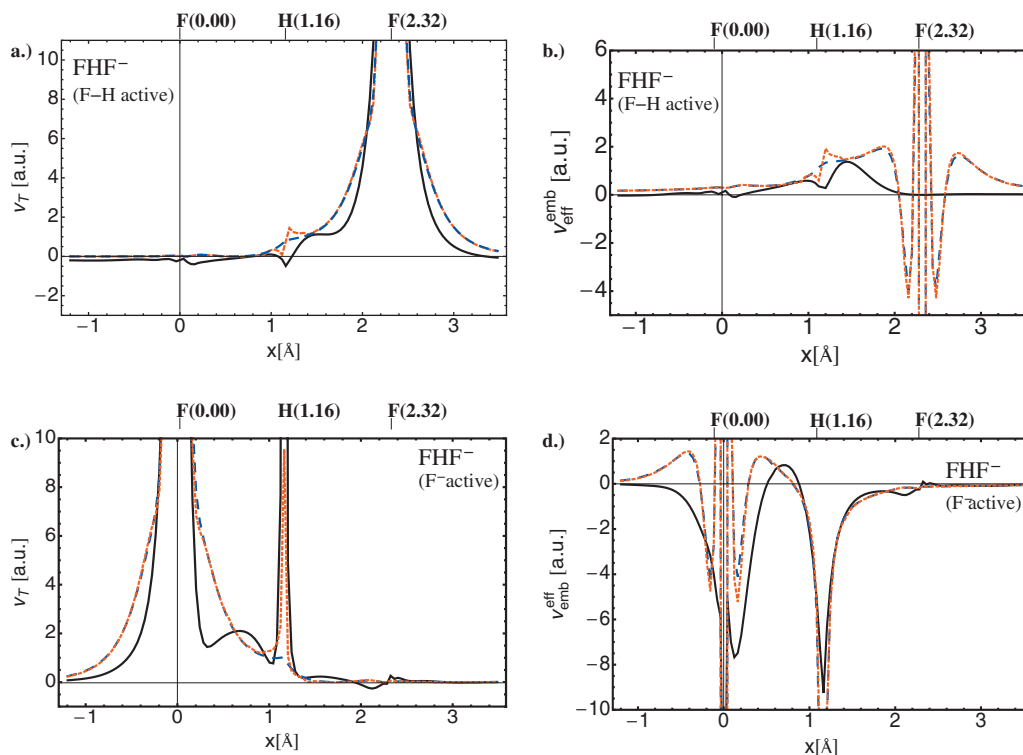


FIG. 7. Comparison of (a) the accurate kinetic-energy component  $v_T(r)$  and (b) the total embedding potentials  $v_{\text{emb}}^{\text{eff}}(r)$  (both black solid line) with approximate potentials obtained using the TF (blue dashed line) and PW91k (red dashed line) functionals for F–H–F<sup>-</sup> with F–H being the active subsystem. [(c) and (d)] Comparison of accurate and approximate potentials for F–H–F<sup>-</sup> with F<sup>-</sup> as active subsystem.

constant between the hydrogen and the fluorine atom of the active subsystem, i.e., the repulsive feature of the accurate embedding potential in the region is not captured. Recall that the accurate and the approximate potentials differ by a constant shift  $\Delta\mu$ , which does not affect the electron density. Again, the approximate kinetic-energy functionals are able to recover the behavior of the accurate reference potential at and close to the nonfrozen subsystem. But when moving closer to the frozen subsystem, they lead to a too repulsive potential, while at the frozen subsystem, they fail to compensate the large nuclear attraction and lead to a too attractive embedding potential. For F–H–F<sup>-</sup> the approximate embedding potentials compared to the accurate potential show larger errors than for the water dimer, but as discussed in Sec. III the electron densities obtained from these approximate potentials are still sufficiently accurate. As for the water dimer, it therefore appears that in the most important regions (i.e., at the nonfrozen subsystem and in between the subsystems) the approximate potentials are reliable.

If we now turn to the case in which the F<sup>-</sup> anion (subsystem 2) is the active subsystem, and in which the electrons forming the hydrogen bond are included in the active subsystem, the accurate potentials shown in Figs. 7(c) and 7(d) are again more complicated than for F–H as active subsystem. The accurate embedding potential is very small at the nonfrozen fluorine atom, becomes more attractive between the subsystems, and shows attractive peaks at the hydrogen atom and at the fluorine atom of the frozen subsystem. Because of the charge transfer between the subsystems accompanied by the formation of the hydrogen

bond, the long-distance limit does no longer apply and the embedding potential deviates from zero at the frozen subsystem.

Again, the approximate potentials obtained with TF and PW91k are almost identical. At the nonfrozen subsystem and in between the subsystems, they reproduce the accurate embedding potential quite accurately. Surprisingly, also at the hydrogen atom of the frozen subsystem, the approximate potentials are very close to the accurate one. Note that even though the kinetic-energy component differs for TF and PW91 at the position of the hydrogen atom, this difference does not show up in the approximate embedding potentials because it is outweighed by the nuclear contribution. At the fluorine atom of the frozen subsystem, the approximate potentials are similar to the ones found when the other subsystem is active, i.e., is overall attractive with oscillations occurring close to the nucleus. Qualitatively, they reproduce the attractive character of the accurate potential, even though their detailed shapes do not match perfectly. Overall, both approximate potentials agree well with the accurate one, in particular, in the important regions in between the subsystems and close to the frozen hydrogen atom.

### C. Ammonia borane

For ammonia borane, the kinetic-energy component  $v_T$  and the effective embedding potential  $v_{\text{emb}}^{\text{eff}}$  for BH<sub>3</sub> is the active subsystem are presented in Figs. 8(a) and 8(b), respectively, while in Figs. 8(c) and 8(d) they are shown for NH<sub>3</sub> as active subsystem. Note that the latter case is notoriously more difficult for approximate functionals because the active

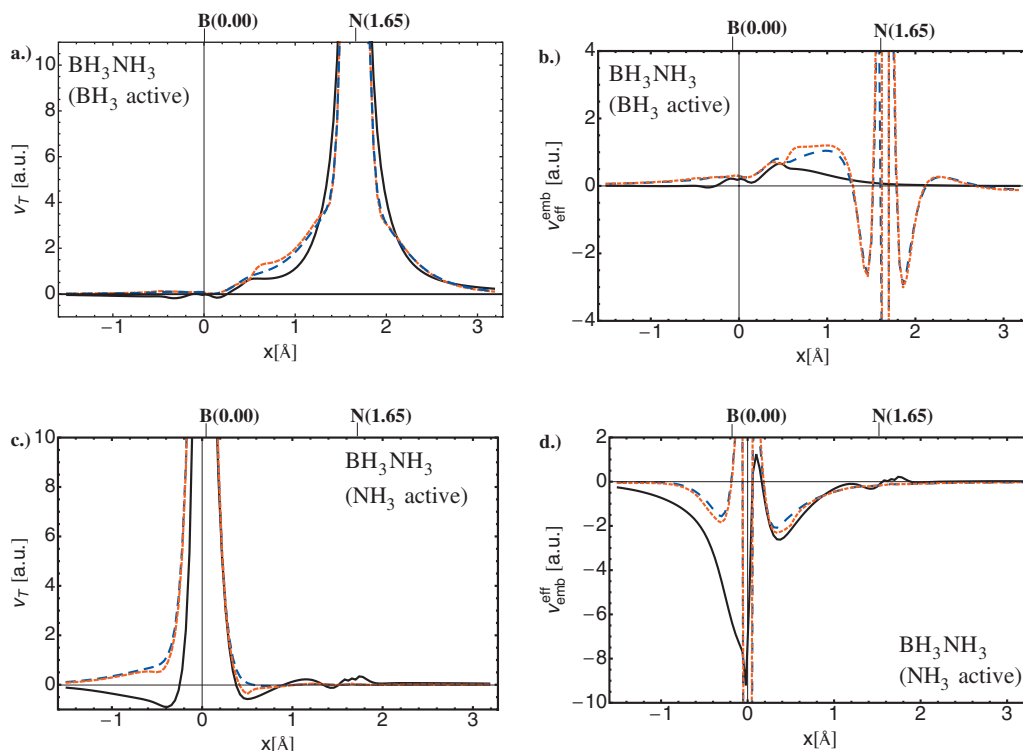


FIG. 8. Comparison of (a) the accurate kinetic-energy component  $v_T(r)$  and (b) the total embedding potentials  $v_{\text{emb}}^{\text{eff}}(r)$  (both black solid line) with approximate potentials obtained using the TF (blue dashed line) and PW91k (red dashed line) functionals for ammonia borane with  $\text{BH}_3$  as active subsystem. [(c) and (d)] Comparison of accurate and approximate potentials for ammonia borane with  $\text{NH}_3$  as active subsystem.

subsystem contains the nitrogen lone pair, which forms the coordination bond to the frozen  $\text{BH}_3$  molecule.

For the case where  $\text{BH}_3$  is the active subsystem, the accurate embedding potential shown in Fig. 8(b) is repulsive between the two subsystems and then drops to zero when approaching the frozen subsystem. The shape of this repulsive feature between the subsystems is similar to the one observed for  $\text{F}-\text{H}-\text{F}^-$ , but less pronounced. This is understandable as the strength of the bond and thus also the amount of electron-density redistribution is significantly weaker.

The approximate embedding potentials are very similar for TF and PW91k. They both approximately recover the accurate reference potential at the nonfrozen subsystem and capture the increase in the repulsive potential between the subsystems, but in contrast to the accurate reference the approximate potentials decrease much slower and significantly overestimate the embedding potential between the subsystems. This too repulsive part of the approximate potentials is more pronounced and appears closer to the active subsystem than for the hydrogen-bonded systems. Therefore, the errors observed in the resulting densities are larger for ammonia borane than for  $\text{F}-\text{H}-\text{F}^-$ . At the frozen subsystem and, in particular, at its nitrogen nucleus, the accurate embedding potential is (almost) zero, i.e., the kinetic-energy component cancels the nuclear attraction. As for the hydrogen-bonded systems, the approximate potentials do not behave correctly at the frozen subsystem but instead they lead to an oscillatory, overall attractive embedding potential.

For  $\text{NH}_3$  as active subsystem [see Figs. 8(c) and 8(d)], where the electron pair forming the coordination bond is

included in the active subsystem, both the kinetic-energy component and the total embedding potential are much more complicated than in the cases considered so far. While the accurate embedding potential is still small at the nonfrozen subsystem, it does not decrease to zero at the nuclei of the frozen subsystem anymore, i.e., the cancellation of the nuclear attraction by the repulsive kinetic-energy component no longer occurs. Instead the embedding potential shows two attractive minima, one between the two subsystems corresponding to an accumulation of electron density in the bonding region and another one at the boron nucleus which is due to the shift of electron density to the frozen subsystem. In between these minima, a weakly repulsive maximum occurs close to the boron nucleus.

Surprisingly, the approximate potentials obtained with the TF and PW91k functionals describe the embedding potential at the nonfrozen subsystem, the minimum occurring between the subsystems, and even the repulsive feature close to the boron nucleus quite accurately. In particular, the minimum is captured somewhat better by PW91k. However, the shape of the embedding potential around the boron nucleus of the frozen subsystem closely resembles the one found for the other systems considered so far: The embedding potential is overall attractive with two sharp repulsive peaks close to the nucleus. However, at the boron nucleus the approximate potentials are not attractive enough and neither of the approximate potentials is able to reproduce shape of the embedding potential at the boron nucleus. In particular, the approximate potentials are rather symmetric with respect the boron nucleus and do not capture the asymmetry of the ac-

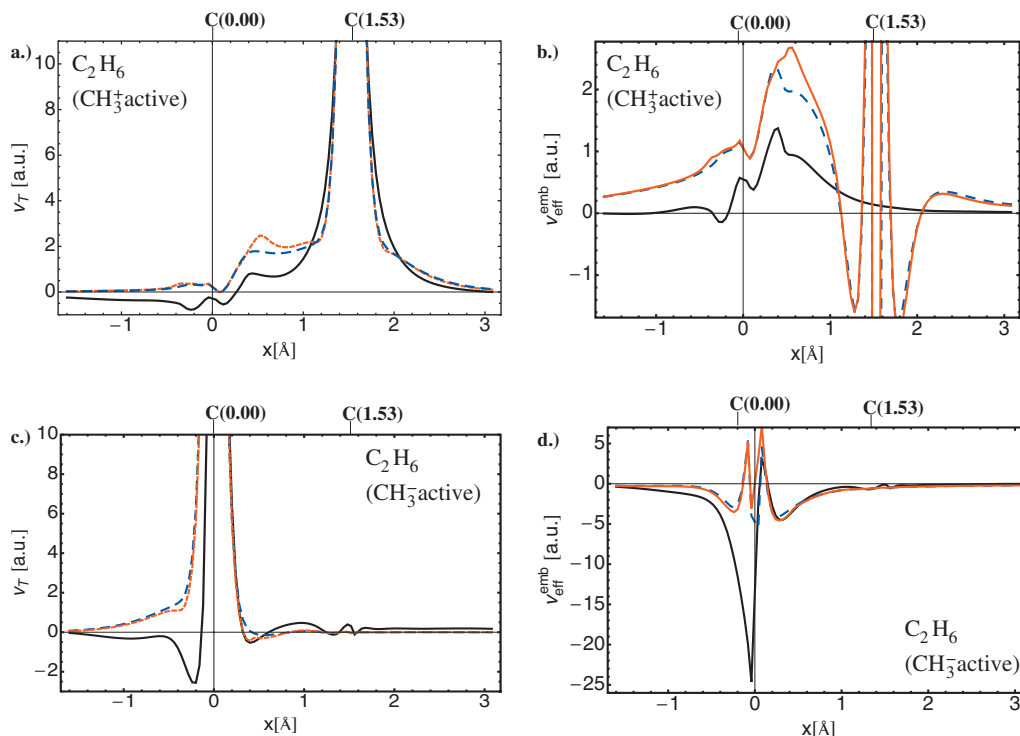


FIG. 9. Comparison of (a) the accurate kinetic-energy component  $v_T(\mathbf{r})$  and (b) the total embedding potentials  $v_{\text{emb}}^{\text{eff}}(\mathbf{r})$  (both black solid line) with approximate potentials obtained using the TF (blue dashed line) and PW91k (red dashed line) functionals for ethane with  $\text{CH}_3^+$  as active subsystem. [(c) and (d)] Comparison of accurate and approximate potentials for ethane with  $\text{CH}_3$  as active subsystem.

curate reference potential. This appears to be the main reason for the insufficiencies of the approximate potentials in describing coordination bonds.

#### D. Ethane

Finally, as the most crucial model system, we consider ethane for which the kinetic-energy component  $v_T$  and the effective embedding potential  $v_{\text{emb}}^{\text{eff}}$  are depicted in Figs. 9(a) and 9(b) for subsystem  $\text{CH}_3^+$  as active subsystem, respectively, as well as in Figs. 9(c) and 9(d) for  $\text{CH}_3$  being the active subsystem. This is the most challenging model system because the two subsystems are connected by a prototypical covalent bond that as discussed above cannot be adequately described in FDE when using approximate kinetic energy functionals. Therefore, the comparison to the accurate reference potentials might give useful insight for the development of improved kinetic-energy functionals.

We start by considering the first case, in which  $\text{CH}_3^+$  is the active subsystem, i.e., the electron pair forming the covalent bond is contained in the frozen density. The reference for the kinetic-energy component  $v_T$  shown in Fig. 9(a) is weakly attractive at the nonfrozen subsystem and as for all other considered model systems strongly repulsive at the frozen subsystem. The accurate embedding potential shown in Fig. 9(b) is qualitatively similar to the one obtained for ammonia borane when the  $\text{BH}_3$  subsystem is active. The embedding potential exhibits two repulsive maxima, one at the carbon atom of the frozen subsystem and one in between the subsystems. It decreases in the following, when going closer to the frozen subsystem and is rather small at the carbon atom of the frozen subsystem. Compared to ammonia bo-

rane, the embedding potential is more repulsive, and in between the subsystems is about twice as large. The approximate embedding potentials are again very similar for the TF and PW91k functionals. At the frozen subsystem and in between the subsystems, the shape of the approximate potentials qualitatively matches the one of the accurate reference potential, whereas in the bonding region, the shape of the potential obtained with PW91k is more similar to the accurate one. However, both for TF and for PW91k the approximate embedding potentials significantly overestimate the magnitude of the embedding potential. At the frozen subsystem, the approximate potential again have a similar form as for the other considered systems. While the accurate potential is small and close to zero, the approximate ones are overall attractive with two sharp repulsive features close to the carbon nucleus of the frozen subsystem.

In the second case shown in Figs. 9(c) and 9(d), where  $\text{CH}_3$  is chosen as the active subsystem which contains the electron pair forming the covalent bond between the subsystems. Qualitatively, the accurate embedding potential shown in Fig. 9(d) is similar to the one found for ammonia borane when  $\text{NH}_3$  is the active subsystem. It is almost zero at the nonfrozen subsystem and overall attractive between the two subsystems and at the frozen subsystem. One finds two attractive minima, one between the subsystems corresponding to the accumulation of charge due to the formation of the covalent bond and one much deeper minimum at the carbon atom of the frozen subsystem corresponding to the charge transfer between the subsystems. In particular, the long-distance limit breaks down and the embedding potential is not small at the frozen subsystem. Surprisingly, the approxi-

mate embedding potentials obtained with TF and with PW91k are both able to reproduce the accurate potential quite accurately in between the subsystems and even capture the maximum close to the frozen carbon atom correctly. However, the attractive potential at this carbon atom is not modeled correctly, but instead the shape of the approximate embedding potential at the frozen subsystem matches the one found for the other model systems. These huge errors of the approximate potentials make it practically impossible to obtain a reasonable description of ethane with approximate FDE.

## VI. CONCLUSIONS AND OUTLOOK

As a first step toward the development of improved approximations of  $v_T$ , in this work we presented accurate reference potentials for the kinetic-energy component  $v_T[\rho_1, \rho_2]$  of the effective embedding potential in the FDE scheme. For this purpose the method of Wu and Yang<sup>62</sup> for the reconstruction of the KS potential from a given input electron density has been implemented. By reconstructing the KS potential corresponding to the correct density of the active subsystem  $\rho_1(\mathbf{r}) = \rho_{\text{tot}}(\mathbf{r}) - \rho_2(\mathbf{r})$ , it was then possible to obtain an accurate  $v_T$  by means of the exact expression derived in Ref. 43.

However, several technical issues had to be addressed. First, since in the potential reconstruction a finite basis set is used for the KS orbitals, and thus also for the electron density, the corresponding KS potential is not unique. Therefore, it is necessary to ensure that smooth, physically meaningful potentials are obtained. In our implementation, this is achieved by employing the method proposed by Bulat *et al.*, which introduces an additional smoothing constraint.<sup>63</sup> Then, a reconstructed potential, that is “as smooth as possible” is obtained. By careful numerical tests we were able to confirm the quality of the reconstructed potentials. Second, the choice of the frozen density  $\rho_2$  turned out to be problematic because it has to be chosen such that the resulting exact  $\rho_1$  is both non-negative everywhere in space and  $v_s$ -representable. In this work, we obtained  $\rho_2$  from selected localized molecular orbitals from the calculation for the full system, which guarantees that the corresponding  $\rho_1$  is non-negative. However, the tails of the localized orbitals lead to nodes in the resulting densities so that  $\rho_1$  is in general not  $v_s$ -representable. Therefore, the reconstruction does not result in the exact  $\rho_1$ , but only in a close approximation to it. Nevertheless, the resulting errors in the density are in all cases significantly smaller than those obtained in approximate FDE calculations. In future work, we will investigate potentially better choices of the frozen density and possibilities for improving a given density partitioning with freeze-and-thaw cycles.

The accurate references for  $v_T$  have then been used to assess the quality of two widely used approximations for  $v_T$ , (i.e., those derived from the TF and PW91k kinetic-energy functionals). For this comparison, we included test systems in which the subsystems are connected by hydrogen bonds of different strengths, by a coordination bond, and by a prototypical covalent bond. The accurate embedding potentials are

qualitatively different when the electron pair forming the bond between the subsystems is included in the active or in the frozen subsystem, respectively. In the latter case, there is, in general, no or only a small amount of electron density from the active subsystem reaching out to the frozen subsystem, i.e., there is no charge transfer between the subsystems. Therefore, the embedding potential at the frozen subsystem is, in general, very small. Only in between the subsystems, the embedding potential significantly deviates from zero and shows repulsive features, which become more pronounced with increasing strength of the bonding interaction between the subsystems. In contrast, when the bonding electrons are included in the active subsystem, there is charge transfer between the subsystems and the accurate embedding potential is attractive at the frozen subsystem and in between the subsystems. The stronger the bonding interaction between the subsystems, the more attractive is the embedding potential at the frozen subsystem.

The approximate embedding potentials obtained with TF and PW91k are not able to distinguish between these two different cases (i.e., charge transfer versus no charge transfer). Instead, the embedding potential close to the second-row atoms in the frozen subsystem is very similar in all cases investigated here. The embedding potential is overall attractive, with sharp repulsive features occurring close to the nucleus. The depth of this embedding potential is similar for all considered model systems and does not depend on the strength of the bonds between the subsystems. On the other hand, close to hydrogen nucleus in the frozen subsystem (for which there are no core electrons to account for), the approximate embedding potential closely resembles the accurate ones. This good agreement explains the success of these approximate potentials for hydrogen-bonded systems.

The two approximate kinetic-energy functionals investigated here, TF and PW91k, lead to very similar embedding potentials, and from our comparison it is not possible to prefer one over the other. Recently, improved nondecomposable approximations to  $v_T$  have been proposed, that should particularly improve the embedding potential at the frozen subsystem. In particular, the correction proposed in Ref. 43 ensures that the embedding potential is zero at the frozen subsystem. However, this is only correct as long as there is no charge transfer. Similarly, the nondecomposable second derivative approximation introduced by Garcia-Lastra *et al.*<sup>44</sup> seeks to improve the embedding potential close to the nuclei of the frozen subsystem by switching on the full von Weizsäcker term close to the nuclei. Because the von Weizsäcker functional has the correct behavior close to the nuclei (i.e., it is able to cancel the nuclear attraction), approximate kinetic-energy functional based on the von Weizsäcker functional (instead of the Thomas–Fermi functional) have a long history<sup>81,82</sup> and might prove useful also for constructing approximations to  $v_T$ . However, a detailed assessment of these and other approximations to  $v_T$  is beyond the scope of this work and will be presented elsewhere. The availability of accurate reference potentials will make it possible to better understand the errors of the currently available approximations and is thus a first step toward the devel-

opment of improved approximations that can also describe covalent interactions between the subsystems.

Finally, we mention that the efficient calculation of accurate embedding potentials is also of great importance in the context of schemes for embedding wave-function theory calculations into environments described by DFT (WFT-in-DFT embedding).<sup>83–92</sup> In contrast to standard FDE calculations, within such schemes performing a DFT calculation on the full system—which is a prerequisite for the reconstruction of an accurate embedding potential—is not a bottleneck because the computationally most expensive part is usually the WFT calculation.<sup>93,94</sup> However, because an accurate description of the virtual orbital space is mandatory for correlated wave-function based calculations, for WFT-in-DFT embedding it is of crucial importance to use smooth embedding potentials of high quality, such as those obtained in this work.

## ACKNOWLEDGMENTS

This work has been supported by the Netherlands Organization for Scientific Research (NWO) via a Rubicon scholarship for C.R.J., a Vidi grant (Grant No. 700.59.422) for J.N., and a Vici grant for L.V. Financial support from ETH Zurich for S.F. and M.R. (Grant No. TH-26 07-3) is gratefully acknowledged.

- <sup>1</sup>J. Neugebauer, *ChemPhysChem* **10**, 3148 (2009).
- <sup>2</sup>J. Neugebauer, *Phys. Rep.* **489**, 1 (2010).
- <sup>3</sup>A. Warshel and M. Levitt, *J. Mol. Biol.* **103**, 227 (1976).
- <sup>4</sup>P. Sherwood, in *Modern Methods and Algorithms of Quantum Chemistry*, NIC Series Vol. 1, edited by J. Grotenдорst (John von Neumann Institute for Computing, Jülich, 2000), pp. 257–277.
- <sup>5</sup>H. M. Senn and W. Thiel, *Top. Curr. Chem.* **268**, 173 (2007).
- <sup>6</sup>H. M. Senn and W. Thiel, *Angew. Chem., Int. Ed.* **48**, 1198 (2009).
- <sup>7</sup>S. C. L. Kamerlin, M. Haranczyk, and A. Warshel, *J. Phys. Chem. B* **113**, 1253 (2009).
- <sup>8</sup>D. W. Zhang and J. Z. H. Zhang, *J. Chem. Phys.* **119**, 3599 (2003).
- <sup>9</sup>D. G. Fedorov and K. Kitaura, *J. Phys. Chem. A* **111**, 6904 (2007).
- <sup>10</sup>T. Nagata, D. G. Fedorov, K. Kitaura, and M. S. Gordon, *J. Chem. Phys.* **131**, 024101 (2009).
- <sup>11</sup>T. A. Wesolowski and A. Warshel, *J. Phys. Chem.* **97**, 8050 (1993).
- <sup>12</sup>P. Cortona, *Phys. Rev. B* **44**, 8454 (1991).
- <sup>13</sup>M. Iannuzzi, B. Kirchner, and J. Hutter, *Chem. Phys. Lett.* **421**, 16 (2006).
- <sup>14</sup>Ch. R. Jacob, J. Neugebauer, and L. Visscher, *J. Comput. Chem.* **29**, 1011 (2008).
- <sup>15</sup>J. Neugebauer, M. J. Louwerse, E. J. Baerends, and T. A. Wesolowski, *J. Chem. Phys.* **122**, 094115 (2005).
- <sup>16</sup>T. A. Wesolowski, in *Computational Chemistry: Reviews of Current Trends*, edited by J. Leszczynski (World Scientific, Singapore, 2006), Vol. 10, pp. 1–82.
- <sup>17</sup>J. Neugebauer, Ch. R. Jacob, T. A. Wesolowski, and E. J. Baerends, *J. Phys. Chem. A* **109**, 7805 (2005).
- <sup>18</sup>J. Neugebauer, M. J. Louwerse, P. Belanzoni, T. A. Wesolowski, and E. J. Baerends, *J. Chem. Phys.* **123**, 114101 (2005).
- <sup>19</sup>Ch. R. Jacob, J. Neugebauer, L. Jensen, and L. Visscher, *Phys. Chem. Chem. Phys.* **8**, 2349 (2006).
- <sup>20</sup>R. E. Bulo, Ch. R. Jacob, and L. Visscher, *J. Phys. Chem. A* **112**, 2640 (2008).
- <sup>21</sup>M. Strajbl, G. Hong, and A. Warshel, *J. Phys. Chem. B* **106**, 13333 (2002).
- <sup>22</sup>M. H. M. Olsson, G. Hong, and A. Warshel, *J. Am. Chem. Soc.* **125**, 5025 (2003).
- <sup>23</sup>G. Hong, E. Rosta, and A. Warshel, *J. Phys. Chem. B* **110**, 19570 (2006).
- <sup>24</sup>Y. Xiang and A. Warshel, *J. Phys. Chem. B* **112**, 1007 (2008).
- <sup>25</sup>T. A. Wesolowski and J. Weber, *Chem. Phys. Lett.* **248**, 71 (1996).
- <sup>26</sup>O. V. Gritsenko, in *Recent Advances in Orbital-Free Density Functional Theory*, edited by T. A. Wesolowski and Y. A. Wang (World Scientific, Singapore, in press).
- <sup>27</sup>J. Neugebauer, *J. Chem. Phys.* **126**, 134116 (2007).
- <sup>28</sup>J. Neugebauer, *J. Phys. Chem. B* **112**, 2207 (2008).
- <sup>29</sup>J. Neugebauer, *J. Chem. Phys.* **131**, 084104 (2009).
- <sup>30</sup>M. E. Casida and T. A. Wesolowski, *Int. J. Quantum Chem.* **96**, 577 (2004).
- <sup>31</sup>T. A. Wesolowski, *J. Am. Chem. Soc.* **126**, 11444 (2004).
- <sup>32</sup>L. H. Thomas, *Proc. Cambridge Philos. Soc.* **23**, 542 (1927).
- <sup>33</sup>E. Fermi, *Z. Phys.* **48**, 73 (1928).
- <sup>34</sup>F. Tran and T. A. Wesolowski, *Int. J. Quantum Chem.* **89**, 441 (2002).
- <sup>35</sup>T. A. Wesolowski, H. Chermette, and J. Weber, *J. Chem. Phys.* **105**, 9182 (1996).
- <sup>36</sup>T. A. Wesolowski, *J. Chem. Phys.* **106**, 8516 (1997).
- <sup>37</sup>A. Lembarki and H. Chermette, *Phys. Rev. A* **50**, 5328 (1994).
- <sup>38</sup>T. A. Wesolowski, Y. Ellinger, and J. Weber, *J. Chem. Phys.* **108**, 6078 (1998).
- <sup>39</sup>T. A. Wesolowski, P.-Y. Morgantini, and J. Weber, *J. Chem. Phys.* **116**, 6411 (2002).
- <sup>40</sup>Ch. R. Jacob, T. A. Wesolowski, and L. Visscher, *J. Chem. Phys.* **123**, 174104 (2005).
- <sup>41</sup>K. Kiewisch, G. Eickerling, M. Reiher, and J. Neugebauer, *J. Chem. Phys.* **128**, 044114 (2008).
- <sup>42</sup>A. W. Götz, S. M. Beyhan, and L. Visscher, *J. Chem. Theory Comput.* **5**, 3161 (2009).
- <sup>43</sup>Ch. R. Jacob, S. M. Beyhan, and L. Visscher, *J. Chem. Phys.* **126**, 234116 (2007).
- <sup>44</sup>J. M. Garcia Lastra, J. W. Kaminski, and T. A. Wesolowski, *J. Chem. Phys.* **129**, 074107 (2008).
- <sup>45</sup>Ch. R. Jacob and L. Visscher, in *Recent Advances in Orbital-Free Density Functional Theory*, edited by T. A. Wesolowski and Y. A. Wang (World Scientific, Singapore, in press).
- <sup>46</sup>S. Fux, K. Kiewisch, Ch. R. Jacob, J. Neugebauer, and M. Reiher, *Chem. Phys. Lett.* **461**, 353 (2008).
- <sup>47</sup>S. M. Beyhan, A. W. Götz, Ch. R. Jacob, and L. Visscher, *J. Chem. Phys.* **132**, 044114 (2010).
- <sup>48</sup>Ch. R. Jacob and L. Visscher, *J. Chem. Phys.* **128**, 155102 (2008).
- <sup>49</sup>P. R. T. Schipper, O. V. Gritsenko, S. J. A. van Gisbergen, and E. J. Baerends, *J. Chem. Phys.* **112**, 1344 (2000).
- <sup>50</sup>O. V. Gritsenko, P. R. T. Schipper, and E. J. Baerends, *Chem. Phys. Lett.* **302**, 199 (1999).
- <sup>51</sup>O. V. Gritsenko, P. R. T. Schipper, and E. J. Baerends, *Int. J. Quantum Chem.* **76**, 407 (2000).
- <sup>52</sup>T. W. Keal and D. J. Tozer, *J. Chem. Phys.* **119**, 3015 (2003).
- <sup>53</sup>T. W. Keal and D. J. Tozer, *J. Chem. Phys.* **121**, 5654 (2004).
- <sup>54</sup>A. Savin and T. A. Wesolowski, in *Advances in the Theory of Atomic and Molecular Systems*, edited by P. Piecuch, J. Maruani, G. Delgado-Barrio, and S. Wilson (Springer, Dordrecht, 2009), pp. 311–326.
- <sup>55</sup>P. Hohenberg and W. Kohn, *Phys. Rev.* **136**, B864 (1964).
- <sup>56</sup>H. Englisch and R. Englisch, *Phys. Status Solidi B* **123**, 711 (1984).
- <sup>57</sup>H. Englisch and R. Englisch, *Phys. Status Solidi B* **124**, 373 (1984).
- <sup>58</sup>S. Liu and P. W. Ayers, *Phys. Rev. A* **70**, 022501 (2004).
- <sup>59</sup>Y. Wang and R. G. Parr, *Phys. Rev. A* **47**, R1591 (1993).
- <sup>60</sup>R. van Leeuwen and E. J. Baerends, *Phys. Rev. A* **49**, 2421 (1994).
- <sup>61</sup>Q. Zhao, R. C. Morrison, and R. G. Parr, *Phys. Rev. A* **50**, 2138 (1994).
- <sup>62</sup>Q. Wu and W. Yang, *J. Chem. Phys.* **118**, 2498 (2003).
- <sup>63</sup>F. A. Bulat, T. Heaton-Burgess, A. J. Cohen, and W. Yang, *J. Chem. Phys.* **127**, 174101 (2007).
- <sup>64</sup>S. Hirata, S. Ivanov, I. Grabowski, R. Bartlett, K. Burke, and J. D. Talman, *J. Chem. Phys.* **115**, 1635 (2001).
- <sup>65</sup>V. N. Staroverov, G. E. Scuseria, and E. R. Davidson, *J. Chem. Phys.* **124**, 141103 (2006).
- <sup>66</sup>T. Heaton-Burgess, F. A. Bulat, and W. Yang, *Phys. Rev. Lett.* **98**, 256401 (2007).
- <sup>67</sup>A. Heßelmann, A. W. Götz, F. della Sala, and A. Görling, *J. Chem. Phys.* **127**, 054102 (2007).
- <sup>68</sup>C. Kollmar and M. Filatov, *J. Chem. Phys.* **127**, 114104 (2007).
- <sup>69</sup>P. W. Ayers and W. Yang, *J. Chem. Phys.* **124**, 224108 (2006).
- <sup>70</sup>Amsterdam density functional program, Theoretical Chemistry, Vrije Universiteit, Amsterdam, URL: <http://www.scm.com>.
- <sup>71</sup>Ch. R. Jacob, R. Bulo, A. W. Götz, S. M. Beyhan, and L. Visscher, *PyADF—a Scripting Framework for Quantum Chemistry* (VU University, Amsterdam/ETH Zurich, Zurich, 2009).
- <sup>72</sup>A. D. Becke, *Phys. Rev. A* **38**, 3098 (1988).

- <sup>73</sup>J. P. Perdew, *Phys. Rev. B* **33**, 8822 (1986).
- <sup>74</sup>S. F. Boys, *Rev. Mod. Phys.* **32**, 296 (1960).
- <sup>75</sup>J. M. Foster and S. F. Boys, *Rev. Mod. Phys.* **32**, 300 (1960).
- <sup>76</sup>C. Edmiston and K. Ruedenberg, *Rev. Mod. Phys.* **35**, 457 (1963).
- <sup>77</sup>J. P. Perdew, in *Electronic Structure of Solids*, edited by P. Ziesche and H. Eschrig (Akademie, Berlin, 1991), p. 11.
- <sup>78</sup>Wolfram Research, Inc., MATHEMATICA Version 6.0.3, Champaign, Illinois, 2005.
- <sup>79</sup>Y. A. Bernard, M. D. Dulak, J. W. Kamiński, and T. A. Wesolowski, *J. Phys. A: Math. Theor.* **41**, 055302 (2008).
- <sup>80</sup>R. Bader, *Atoms in Molecules* (Clarendon, Oxford, 1990).
- <sup>81</sup>P. K. Acharya, L. J. Bartolotti, S. B. Sears, and R. G. Parr, *Proc. Natl. Acad. Sci. U.S.A.* **77**, 6978 (1980).
- <sup>82</sup>J. L. Gázquez and J. Robles, *J. Chem. Phys.* **76**, 1467 (1982).
- <sup>83</sup>N. Govind, Y. A. Wang, A. J. R. da Silva, and E. A. Carter, *Chem. Phys. Lett.* **295**, 129 (1998).
- <sup>84</sup>N. Govind, Y. A. Wang, and E. A. Carter, *J. Chem. Phys.* **110**, 7677 (1999).
- <sup>85</sup>T. Klüner, N. Govind, Y. A. Wang, and E. A. Carter, *Phys. Rev. Lett.* **86**, 5954 (2001).
- <sup>86</sup>T. Klüner, N. Govind, Y. A. Wang, and E. A. Carter, *J. Chem. Phys.* **116**, 42 (2002).
- <sup>87</sup>P. Huang and E. A. Carter, *J. Chem. Phys.* **125**, 084102 (2006).
- <sup>88</sup>P. Huang and E. A. Carter, *Nano Lett.* **6**, 1146 (2006).
- <sup>89</sup>P. Huang and E. A. Carter, *Nano Lett.* **8**, 1265 (2008).
- <sup>90</sup>S. Sharifzadeh, P. Huang, and E. Carter, *J. Phys. Chem. C* **112**, 4649 (2008).
- <sup>91</sup>S. Sharifzadeh, P. Huang, and E. A. Carter, *Chem. Phys. Lett.* **470**, 347 (2009).
- <sup>92</sup>A. S. P. Gomes, Ch. R. Jacob, and L. Visscher, *Phys. Chem. Chem. Phys.* **10**, 5353 (2008).
- <sup>93</sup>O. Roncero, M. P. de Lara-Castells, P. Villarreal, F. Flores, J. Ortega, M. Paniagua, and A. Aguado, *J. Chem. Phys.* **129**, 184104 (2008).
- <sup>94</sup>O. Roncero, A. Zanchet, P. Villarreal, and A. Aguado, *J. Chem. Phys.* **131**, 234110 (2009).